

Emergent Mesoscale Phenomena in Magnetized Accretion Disc Turbulence

Jacob B. Simon^{1*}, Kris Beckwith^{1,3*}, Philip J. Armitage^{1,2†}

¹JILA, University of Colorado & NIST, 440 UCB, Boulder, CO 80309-0440

²Department of Astrophysical and Planetary Sciences, University of Colorado at Boulder

³Tech-X Corporation, 5621 Arapahoe Ave. Suite A Boulder, CO 80303

Email: *jbsimon@jila.colorado.edu, *kris.beckwith@jila.colorado.edu, †pja@jila1.colorado.edu

24 February 2013

ABSTRACT

We study how the structure and variability of magnetohydrodynamic (MHD) turbulence in accretion discs converge with domain size. Our results are based on a series of vertically stratified local simulations, computed using the *Athena* MHD code, that have fixed spatial resolution, but varying radial and azimuthal extent (from $\Delta R = 0.5H$ to $16H$, where H is the vertical scale height). We show that elementary local diagnostics of the turbulence, including the Shakura-Sunyaev α parameter, the ratio of Maxwell stress to magnetic energy, and the ratio of magnetic to fluid stresses, converge to within the precision of our measurements for spatial domains of radial size $L_x \geq 2H$. We obtain $\alpha \simeq 0.02 - 0.03$, consistent with other recent determinations. Very small domains ($L_x = 0.5H$) return anomalous results, independent of spatial resolution. This convergence with domain size, however, is only valid for a limited set of diagnostics: larger spatial domains admit the emergence of dynamically important mesoscale structures. In our largest simulations, the Maxwell stress shows a significant large scale non-local component, while the density develops long-lived axisymmetric perturbations (“zonal flows”) at the 20% level. Most strikingly, the variability of the disc in fixed-sized patches decreases strongly as the simulation volume increases, while variability in the magnetically dominated corona remains constant. Comparing our largest local simulations to global simulations with comparable spatial resolution, we find generally good agreement. There is no direct evidence that the presence of curvature terms or radial gradients in global calculations materially affect the turbulence, except to perhaps introduce an outer radial scale for mesoscale structures. The demonstrated importance of mean magnetic fields – seen in both large local and global simulations – implies, however, that the growth and saturation of these fields is likely of critical importance for the evolution of accretion discs.

Key words: accretion, accretion discs – MHD – instabilities – turbulence

1 INTRODUCTION

Accretion of gas through a disc onto a central object plays a pivotal role in the formation of protostars and planets, and furnishes the only probe of the environment around black holes to date. If the disc is sufficiently ionized, accretion is driven by a powerful instability that is present in orbiting, magnetized gas: the magnetorotational instability (MRI; Balbus & Hawley 1998, 1991; Blaes & Balbus 1994; Goodman & Xu 1994). The MRI gives rise to sustained magnetohydrodynamic (MHD) turbulence in which the turbulent fluctuations are correlated to produce a positive stress tensor and thus the outward angular momentum transport necessary for the gas to accrete. While numerous analytic investigations of

the MRI’s linear regime (e.g., Balbus & Hawley 1991; Blaes & Balbus 1994) have been insightful, a complete understanding of turbulent disc accretion requires the ability to probe the fully nonlinear behavior of this instability. This is best done through the use of numerical simulations (though, some analytic work in the non-linear regime has been done; Goodman & Xu 1994; Pessah & Goodman 2009).

Numerical studies of accretion discs can be either global or local. These classes of simulations are distinguished by the different length scales that are captured. A local patch of accretion disc can be characterized by two length scales: the distance from the central object, R_0 and the local scale height (disc thickness), $H \approx c_s/\Omega$ (where c_s and Ω are the sound speed and angular velocity at R_0 , respectively). If we asso-

ciate the domain of a simulation with a length scale, L , then local simulations are characterized by $H \sim L \ll R_0$, whereas global simulations are characterized by $H \ll L \sim R_0$.

Local simulations invariably employ the shearing box approximation (e.g., [Hawley et al. 1995](#); [Brandenburg et al. 1995](#)), in which the MHD equations are solved in the frame of a local, co-rotating patch of the disc. The assumption that $H \sim L \ll R_0$ allows the use of a Cartesian geometry while retaining the essential dynamics of differential rotation. This simplifies the problem down to its basic ingredients, orbital shear and magnetization, allowing one to answer basic questions about MRI-driven turbulence, such as “what determines the amplitude of turbulent fluctuations?” At fixed computational cost, local simulations provide the best resolution of small-scale features in the turbulence, which is particularly advantageous if one wishes to study processes such as resistivity or viscosity that are physically important only for $l \ll H$. Local simulations can in principle be simplified yet further by ignoring the vertical component of gravity (“unstratified” simulations). However, in our current work, we only consider stratified calculations which include the vertical gravity from the central object.

Global simulations (e.g., [Armitage 1998](#); [Hawley 2000](#)), on the other hand, evolve a domain that is comparable to the distance from the central object. These simulations are not only typically larger in spatial extent than local models – which may be important if for example long wavelength radial and azimuthal fluctuations are present in the disc – they also include new physical effects. In particular, global models include terms associated with disc curvature, and possess the asymmetry between inward and outward radial directions that is needed to explicitly represent mass accretion. However, these advantages come at the expense of non-trivial “inner” and “outer” boundary conditions. For example, with the exception of black hole disk simulations, where an outflow boundary is applied at the inner boundary to account for material plummeting into an event horizon, particular methods (e.g., viscous or magnetic damping) have to be employed to reduce spurious effects from these boundaries. Global simulations also suffer from poor resolution of small scales, such that most global simulations to-date fail to meet the minimum requirements for numerical convergence that have been derived from local models ([Hawley et al. 2011](#)). Only recently have increases in computational power and algorithmic improvements made it possible to compute global simulations at the resolutions required to adequately resolve the MRI at the level done in local simulations ([Noble et al. 2010](#); [Beckwith et al. 2011](#); [Sorathia et al. 2011](#)).

The near congruence of resolutions between local and global simulations makes possible a comparison of the turbulent properties in these two regimes. One question is whether a local patch of a well-resolved global simulation resembles an equivalently resolved local simulation? If not, are any discrepancies due solely to the different sizes of the domains, or are they instead attributable to truly global effects such as curvature? One approach to addressing this question is to inspect the properties of local sub-domains within a global simulation and compare the statistical properties of these sub-domains to results from shearing boxes ([Sorathia et al. 2010, 2011](#)). These studies suggest that some of the basic properties of local MRI turbulence, such as the relationship between turbulent stress and magnetic flux through a local patch ([Hawley](#)

[et al. 1995](#)) and the tilt angle of the magnetic field autocorrelation function ([Guan et al. 2009](#)), carry over to global calculations.

A complementary approach is to examine the properties of turbulence in large “mesoscale” simulations, characterized by $H \ll L \ll R_0$ ([Guan & Gammie 2011](#)). These simulations, which continue to utilize the shearing box approximation and are in this sense still local, allow study of the influence of long wavelength azimuthal and radial modes on the properties of the turbulence, while also capturing small scale turbulent fluctuations. Compared to global simulations, the mesoscale neglects the effect of curvature terms on the disc, which, in principle, allows the influence of these terms to be elucidated. [Guan & Gammie \(2011\)](#) (see also [Davis et al. 2010](#)) find that, in the mesoscale regime, turbulence is characterized by small scale fluctuations regardless of domain size. These authors also find that, away from the mid-plane, in the coronal region, the magnetic field is correlated on scales of $\sim 10H$ but does not contribute significantly to angular momentum transport. Larger scales are not, however, unimportant. [Nelson & Gressel \(2010\)](#) (see also [Gressel et al. 2011](#); [Yang et al. 2011](#)) demonstrate that long wavelength (again $\gg H$) density correlations determine the amplitude of stochastic density fluctuations (spiral density waves), while the calculations of [Johansen et al. \(2009\)](#) show long lived density/pressure zonal flows in geostrophic balance.

Our goal in this work is to systematically study how the properties of disc turbulence change as one transitions from the local to the mesoscale regime. We do so through a series of shearing box simulations of increasing domain size, from $L_x = 0.5H \times L_y = 2H \times L_z = 8H$ to $L_x = 16H \times L_y = 32H \times L_z = 8H$ (here x , y and z refer to the radial, azimuthal, and vertical directions respectively)¹. In particular, we wish to answer the following questions. How do various properties of MRI-driven turbulence depend on box size? As we push towards the mesoscale regime, what if any phenomena emerge at these larger scales? Is there a scale at which the turbulent properties resemble those in a global disc calculation?

The rest of this paper is structured as follows. In §2, we give details of the numerical algorithm used to integrate the equations of ideal MHD in the local limit and the initial and boundary conditions used for the simulations. In §3, we detail the properties of the quasi-stationary turbulent state via volume-averaged quantities and the vertical structure of the turbulence. In §4, we examine the properties of mesoscale structures within the magnetic field and the implications for the locality of angular momentum transport. The derived variability of accretion is examined in §5. In §6 we compare a subset of our results to those obtained from well-resolved global simulations. Finally, in §7, we summarize our results and discuss implications for the physics of magnetized accretion discs.

¹ Whether the neglect of radial gradients and curvature terms in our large local boxes is physically justified depends upon the geometric thickness of the disc being modeled: a domain of radial scale $\gg H$ remains “local” in thin regions of an AGN disc where $H/R \leq 10^{-2}$, whereas the same would not be true of a thicker protoplanetary disc. Our primary interest in the large boxes is as well-controlled model systems, though the actual value of H/R should be borne in mind when comparing our results to global simulations.

2 METHOD

2.1 Numerical Algorithm

For these calculations, we use *Athena*, a second-order accurate Godunov flux-conservative code for solving the equations of MHD. *Athena* uses the dimensionally unsplit corner transport upwind (CTU) method of [Colella \(1990\)](#) coupled with the third-order in space piecewise parabolic method (PPM) of [Colella & Woodward \(1984\)](#) and a constrained transport (CT; [Evans & Hawley 1988](#)) algorithm for preserving the $\nabla \cdot \mathbf{B} = 0$ constraint. We use the HLLD Riemann solver to calculate the numerical fluxes ([Miyoshi & Kusano 2005](#); [Mignone 2007](#)). A detailed description of the *Athena* algorithm and the results of various test problems are given in [Gardiner & Stone \(2005\)](#), [Gardiner & Stone \(2008\)](#), and [Stone et al. \(2008\)](#).

The simulations use the shearing box approximation, a model for a local co-rotating disc patch whose size is small compared to the radial distance from the central object, R_0 . We construct a local Cartesian frame, $x = (R - R_0)$, $y = R_0\phi$, and z , co-rotating with an angular velocity Ω corresponding to the orbital frequency at R_0 , the center of the box. In this frame, the equations of motion become ([Hawley et al. 1995](#)):

$$\begin{aligned} \frac{\partial \rho}{\partial t} + \nabla \cdot (\rho \mathbf{v}) &= 0 \\ \frac{\partial \rho \mathbf{v}}{\partial t} + \nabla \cdot (\rho \mathbf{v} \mathbf{v} - \mathbf{B} \mathbf{B}) + \nabla \left(P + \frac{1}{2} B^2 \right) &= 2q\rho\Omega^2 \mathbf{x} - \rho\Omega^2 \mathbf{z} - 2\Omega \times \rho \mathbf{v} \\ \frac{\partial \mathbf{B}}{\partial t} - \nabla \times (\mathbf{v} \times \mathbf{B}) &= 0 \end{aligned} \quad (1)$$

where ρ is the mass density, $\rho \mathbf{v}$ is the momentum density, \mathbf{B} is the magnetic field, P is the gas pressure, and q is the shear parameter, defined as $q = -d\ln\Omega/d\ln R$. We use $q = 3/2$, appropriate for a Keplerian disc. We assume an isothermal equation of state $P = \rho c_s^2$, where c_s is the isothermal sound speed. From left to right, the source terms in the momentum equation correspond to radial tidal forces (gravity and centrifugal), vertical gravity, and the Coriolis force. Note that our system of units has the magnetic permeability $\mu = 1$.

The numerical integration of the shearing box equations require additions to the *Athena* algorithm, the details of which can be found in [Stone & Gardiner \(2010\)](#) and in the Appendix of [Simon et al. \(2011\)](#). Briefly, we utilize Crank-Nicholson differencing to conserve epicyclic motion exactly and orbital advection to subtract off the background shear flow ([Stone & Gardiner 2010](#)). The y boundary conditions are strictly periodic, whereas the x boundaries are shearing periodic ([Hawley et al. 1995](#); [Simon et al. 2011](#)). The vertical boundaries are the outflow boundary conditions described in [Simon et al. \(2011\)](#).

2.2 Simulation Parameters and Initial Conditions

All of our simulations are vertically stratified, with an initial density corresponding to isothermal hydrostatic equilibrium.

$$\rho(x, y, z) = \rho_0 \exp\left(-\frac{z^2}{H^2}\right), \quad (2)$$

Table 1. Shearing Box Simulations

Label	Domain Size ($L_x/H \times L_y/H \times L_z/H$)	Resolution (zones/ H)	Initial Field Configuration
FT0.5	$0.5 \times 2 \times 8$	32	Flux tube
FT0.5m	$0.5 \times 2 \times 8$	72	Flux tube
FT0.5h	$0.5 \times 2 \times 8$	144	Flux tube
FT2	$2 \times 4 \times 8$	32	Flux tube
FT4	$4 \times 8 \times 8$	32	Flux tube
FT8	$8 \times 16 \times 8$	32	Flux tube
Y16	$16 \times 32 \times 8$	36	Toroidal

Here, the scale height is defined as $H = \sqrt{2}c_s/\Omega$.

where $\rho_0 = 1$ is the mid-plane density, and H is the scale height in the disc,

$$H = \frac{\sqrt{2}c_s}{\Omega}. \quad (3)$$

The isothermal sound speed, $c_s = 7.07 \times 10^{-4}$, corresponding to an initial value for the mid-plane gas pressure of $P_0 = 5 \times 10^{-7}$. With $\Omega = 0.001$, the value for the scale height is $H = 1$. A density floor of 10^{-4} (10^{-6} for the smallest domain run) is applied to the physical domain as too small a density leads to a large Alfvén speed and a very small timestep. Furthermore, numerical errors make it difficult to evolve regions of very small plasma β .

The initial magnetic field configuration for most of our calculations is the twisted azimuthal flux tube of [Hirose et al. \(2006\)](#), with minor modifications to the dimensions and β values. In particular, the initial toroidal field, B_y , is given by

$$B_y = \begin{cases} \sqrt{\frac{2P_0}{\beta_y} - (B_x^2 + B_z^2)} & \text{if } B_x^2 + B_z^2 \neq 0 \\ 0 & \text{if } B_x^2 + B_z^2 = 0 \end{cases} \quad (4)$$

with $\beta_y = 100$. The poloidal field components, B_x and B_z , are calculated from the y component of the vector potential,

$$A_y = \begin{cases} -\sqrt{\frac{2P_0}{\beta_p} \frac{R_0}{\pi}} \left[1 + \cos\left(\frac{\pi r}{R_0}\right) \right] & \text{if } r < R_0 \\ 0 & \text{if } r \geq R_0 \end{cases} \quad (5)$$

where $r = \sqrt{x^2 + z^2}$ and $\beta_p = 1600$ is the poloidal field β value. We choose R_0 to always be one fourth of the radial domain size; $R_0 = L_x/4$. Figure 1 shows a rendering of the initial magnetic field configuration from FT4.

For the largest domain size, the aspect ratio is such that $R_0 = L_z/2$. As was evident from an initial run at this size and with the flux tube field geometry, the flux tube cannot be properly contained within the domain without initial and dominant boundary condition effects. Thus, we chose our largest domain run, Y16, to be initialized with a constant $\beta = 100$ toroidal field throughout the entire domain. For all of our calculations, random perturbations are added to the density and velocity components to seed the MRI. Table 1 lists the simulations that we have analyzed for this work. The label for each calculation describes the initial field geometry and the x domain size. So, for run FT0.5, FT denotes the flux tube geometry, and the 0.5 denotes $L_x = 0.5H$. As shown in the table, we have also run two higher resolution simulations equivalent to FT0.5; FT0.5m is carried out at 72 zones per H and FT0.5h is carried out at 144 zones per H .

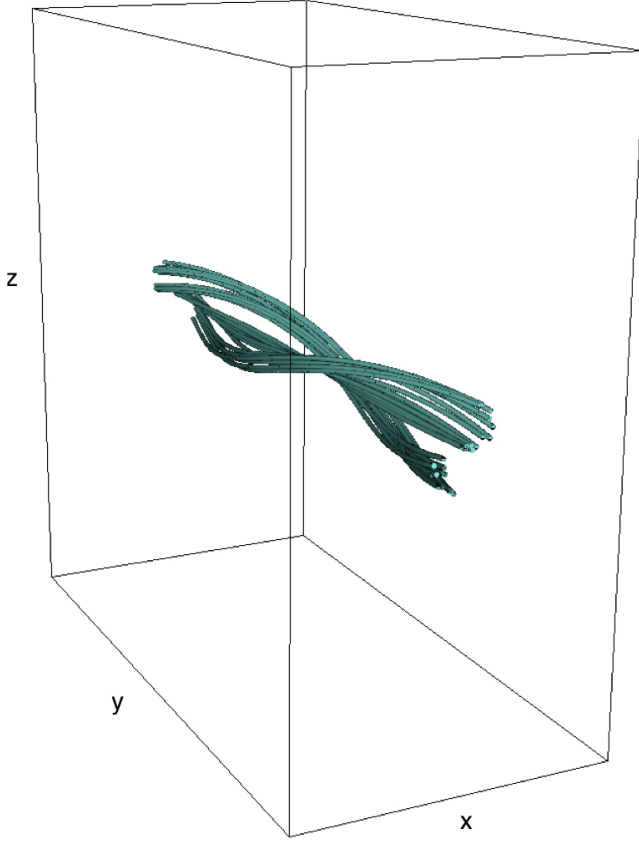


Figure 1. Rendering of the initial magnetic field lines for the FT4 run. This is the twisted azimuthal flux tube of [Hirose et al. \(2006\)](#), and it is the initial field configuration for all of our runs except for Y16.

3 CHARACTERIZING THE TURBULENT STEADY STATE

Although the focus of the current study is on the convergence of the properties of disc turbulence with varying domain size, this can only be meaningful if the simulations being compared have adequate spatial resolution. To satisfy ourselves that this is the case, we first compute the quality parameter Q_j ([Hawley et al. 2011](#)), which characterizes the effective numerical resolution of the turbulence (i.e., how well-resolved the turbulence is). For a direction $j = y, z$, the quality parameter is defined as,

$$Q_j = \frac{2\pi|v_A|}{\Omega\Delta x_j}; \quad |v_A| \equiv \frac{\langle B_j^2 \rangle}{\langle \rho \rangle}. \quad (6)$$

where Δx_j is the grid cell spacing along direction j . Here, the brackets denote a volume average for all x and y and for $|z| < 2H$, and the overbar is a time average from orbit 50 onwards. [Sano et al. \(2004\)](#) demonstrate that $Q \sim 6$ is required in order for the MRI to be well-resolved in the saturated state (though this value is likely to be code-dependent). The values of Q measured for our simulations are given in the final two columns of Table 2. All of the simulations are well-resolved according to this criterion.

Turning to physical rather than numerical quantities, we examine the total (Maxwell plus Reynolds) stress normalized to the gas pressure. The time evolution of this measure, which is equivalent to the α -parameter introduced by [Shakura &](#)

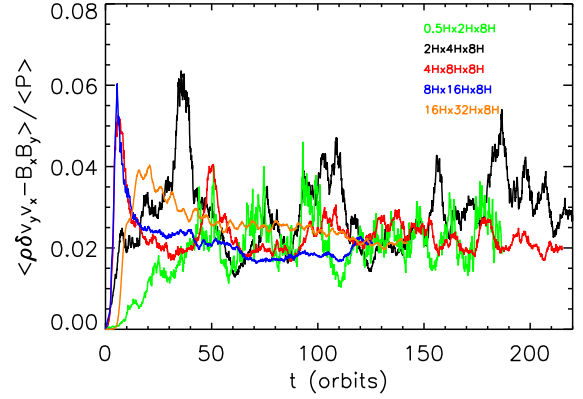


Figure 2. Time history of volume-averaged Maxwell and Reynolds stresses normalized by the volume-averaged pressure for each shearing box domain size. The volume average is done for all x and y and for $|z| < 2H$. The saturation level is roughly consistent between all of the calculations.

Table 2. Saturation Characteristics

Run	α	α_{mag}	MR	BR_x	BR_y	BR_z	Q_y	Q_z
FT0.5	0.022	0.16	4.6	0.056	0.92	0.022	67	10
FT0.5m	0.030	0.13	4.7	0.057	0.92	0.024	188	30
FT0.5h	0.032	0.22	5.5	0.096	0.86	0.045	297	67
FT2	0.027	0.38	3.8	0.11	0.84	0.051	44	11
FT4	0.023	0.40	3.5	0.11	0.84	0.048	39	9
FT8	0.020	0.41	3.4	0.11	0.85	0.045	35	8
Y16	0.024	0.40	3.5	0.12	0.83	0.050	44	11

Here, α is the ratio of stress to gas pressure (i.e., the traditional [Shakura & Sunyaev \(1973\)](#) α parameter), α_{mag} is the ratio of Maxwell stress to magnetic energy, MR is the Maxwell to Reynolds stress ratio, BR_i is the ratio of magnetic energy component i to the total magnetic energy, and Q_i is the quality parameter along direction i as defined via equation (6).

[Sunyaev \(1973\)](#), is shown in Figure 2, where we have volume-averaged the data over all x and y and for $|z| < 2H$. Following an initial transient period, which lasts for the first ~ 50 orbits of the evolution, the normalized stress levels are all roughly equal between different domain sizes. There is, however, a dramatic change in temporal variability as one goes to larger box sizes. This effect was present in the simulations of [Davis et al. \(2010\)](#), and we will discuss it in detail in §5.

The data of Figure 2 allow us to define a time-period, after the 50-orbit mark, where the flow is in a quasi-stationary turbulent state. We use the simulation data from this period to construct various time- and volume-averaged measures of the turbulence (where the volume-average is again performed for all x and y and for $|z| < 2H$). We consider the following diagnostics that characterize the *physical* state of the turbulence:

$$\alpha \equiv \frac{\langle \rho v_x \delta v_y - B_x B_y \rangle}{\langle P \rangle}; \quad \alpha_{\text{mag}} \equiv \frac{2\langle -B_x B_y \rangle}{\langle B^2 \rangle} \quad (7)$$

$$\text{MR} \equiv \frac{\langle -B_x B_y \rangle}{\langle \rho v_x \delta v_y \rangle}; \quad \text{BR}_i \equiv \frac{\langle B_i^2 \rangle}{\langle B^2 \rangle}.$$

These are, in turn, the traditional [Shakura & Sunyaev \(1973\)](#) α parameter; the ratio of Maxwell stress to magnetic energy, α_{mag} ([Hawley et al. 2011](#))²; the ratio of Maxwell to Reynolds stress, MR; and the ratio of magnetic energy component i to the total magnetic energy, BR_i . The angled brackets denote a volume average, whereas the overbars indicate a time average. These quantities are shown in Figure 3 and in Table 2. We find that, within the precision possible given the limited duration of our simulations, all of these metrics appear to converge for domain sizes $L_x \geq 2H$, i.e. for all but the smallest domain. We find that α varies between 0.02 – 0.03; $\alpha_{\text{mag}} \sim 0.4$, consistent with expectations for converged MRI turbulence ([Hawley et al. 2011](#); [Sorathia et al. 2011](#)); the ratio of Maxwell to Reynolds stresses is $\sim 3 - 4$; while finally $\text{BR}_x \sim 0.11$, $\text{BR}_y \sim 0.84$, $\text{BR}_z \sim 0.05$. These diagnostics can be directly compared with the results of [Beckwith et al. \(2011\)](#), who characterized the properties of MRI-driven MHD turbulence in a well-resolved *global* simulation. In that work, the authors found that disc-turbulence measured in regions well away from the innermost stable circular orbit was characterized by $\alpha \sim 0.025$ (directly in the middle of the range found here), $\alpha_{\text{mag}} \sim 0.3$ and finally $\text{BR}_x \sim 0.1$, $\text{BR}_y \sim 0.88$, $\text{BR}_z \sim 0.02$. We conclude that the basic measures of the turbulence reported here are broadly consistent with those in [Beckwith et al. \(2011\)](#).

While boxes larger than $2H \times 4H \times 8H$ show high levels of convergence in these diagnostics, the behaviour of the smallest box (FT0.5) is quite different. While $\alpha = 0.022$ in this case, consistent with the other domain sizes presented here, the other diagnostics are significantly outside of the range of parameter space occupied by the larger domains. Most tellingly, we find that α_{mag} is a factor 2.5 *smaller* than the expected value for converged MRI turbulence ([Hawley et al. 2011](#); [Sorathia et al. 2011](#)). We have verified this behavior for calculations with the same domain size but with 72 and 144 zones per H (see Table 2). The run FT0.5h appears to have values closer to the converged values. However, analyzing the time history of these quantities show that they are not quite saturated between orbit 50 and the end of the calculation. In particular, α_{mag} is still decreasing during the period over which we average. Given limited computational resources, we did not run this case out further, but instead we expect that α_{mag} will saturate at a value lower than that presented here. The bottom line is the anomalous behavior of the small domain simulations is *not* a resolution effect.

The turbulence in the quasi-stationary state can be further characterized by the vertical structure of the simulated disc. In [Simon et al. \(2011\)](#), we examined the statistical distribution of turbulent velocity fluctuations as a function of height above the midplane in runs FT2, FT4, FT8 and Y16, and showed that there was a non-negligible supersonic component for $|z| \gtrsim 3H$ (see Fig. 3 of [Simon et al. 2011](#)). In run

² This is closely related to the “tilt-angle” measured by several authors ([Guan et al. 2009](#); [Beckwith et al. 2011](#); [Sorathia et al. 2011](#)).

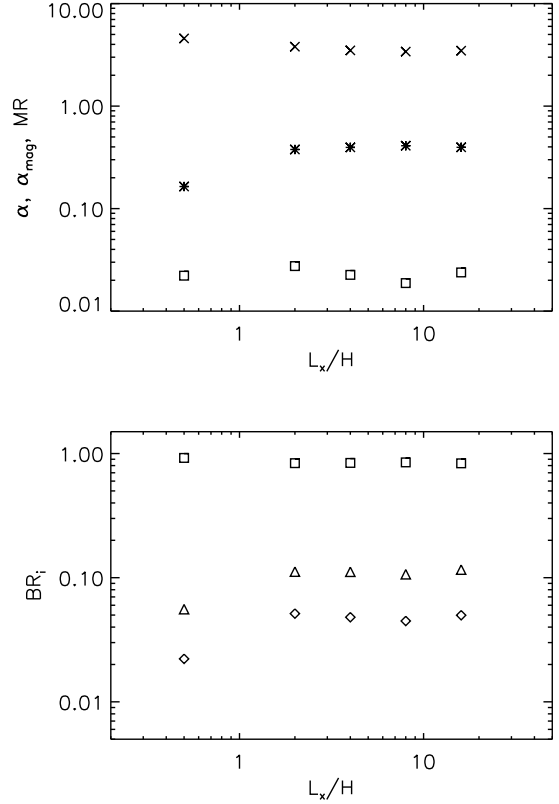


Figure 3. Several time- and volume-averaged quantities versus radial domain size. The left panel displays α (squares), α_{mag} (asterisks), and MR (x's), whereas the right panel displays BR_y (squares), BR_x (triangles), and BR_z (diamonds). These diagnostics are defined by equation (7) and converge for $L_x/H \gtrsim 2$.

FT2 and FT4, this component occupied $\sim 1\%$ and $\sim 5\%$ of the probability distribution space respectively, while for simulations FT8 and Y16, the contribution of supersonic velocity fluctuations converged at $\sim 10\%$ of the probability distribution space, highlighting the possibility of *observable* differences between local and mesoscale treatments of magnetized accretion disc turbulence.

Fig. 4 shows the vertical structure of the total stress normalized to the initial mid-plane gas pressure and the gas $\beta = 2P/B^2$ parameter in the quasi-stationary state. Here, the numerator and denominator for these quantities are time- (from orbit 50 onward) and horizontally-averaged separately before computing their ratio. With the exception of the smallest domain run, the vertical structure appears reasonably consistent between the various domain sizes; the stress is relatively flat until $|z| \sim 2H$, after which it drops off rapidly, and $|z| \sim 2H$ is also where the $\beta \sim 1$ line is crossed. The smallest domain again appears pathological in comparison to the larger domain sizes: the stress is sharply concentrated towards the midplane, where the disc is weakly magnetized ($\beta \sim 20$ cf. $\beta \sim 40$ in the larger domains), while $\beta \lesssim 1$ for $|z| \gtrsim 2H$.

Fig. 5 shows the vertical profile of the energy density in toroidal, radial and vertical magnetic fields normalized to the total magnetic energy density, e.g. $\langle B_i^2 \rangle / \langle B^2 \rangle$ ($i =$

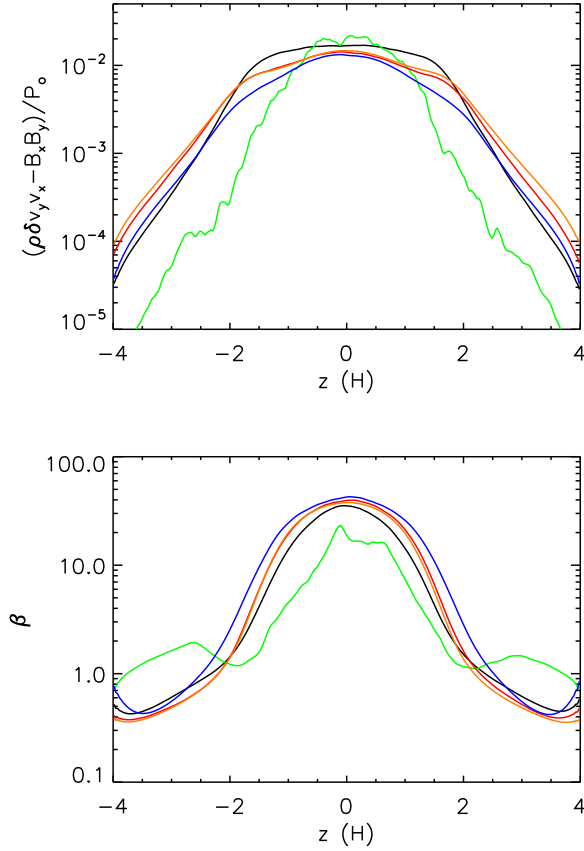


Figure 4. Time- and horizontally-averaged vertical profiles of the total stress normalized to the initial mid-plane gas pressure (top panel) and gas $\beta = 2P/B^2$ parameter (bottom panel). In both cases, the numerator and denominator are separately averaged. The green curve is from FT0.5, black is FT2, red is FT4, blue is FT8, and orange is Y16. With the exception of the smallest domain, the vertical structure of these quantities are consistent between all calculations: the stress is relatively flat until $|z| \sim 2H$, after which it drops off rapidly, and $|z| \sim 2H$ is also where the $\beta \sim 1$ line is crossed.

x, y, z). As before, we average these quantities separately before taking their ratio and we omit data from the smallest domain (run FT0.5) for the purposes of clarity. As was the case with the data shown in Figure 4, the vertical structure of these quantities appear to be reasonably consistent between the various domain sizes: the energy density in toroidal fields dominates throughout the domain. In the region $|z| \lesssim 2H$, the ratio of energy densities is 4 : 40 : 1 ($x : y : z$), while in the region $|z| \gtrsim 3H$, the energy density in vertical fields exceeds that in radial fields, becoming comparable to (but still smaller than) the energy density in toroidal fields. This leads us to an interesting point: the largest domain (Y16) has vertical magnetic field strengths at $|z| = 4H$ that exceed the strength of the radial magnetic field here by a factor ~ 2 and are within a factor of ~ 2 of the toroidal magnetic field strength. Given the vertical gradients of each component of the magnetic field strength, it appears that the energy density in vertical fields will exceed that in toroidal magnetic fields by $|z| = 6H$; such a configuration could lead to angular momentum transport loss through a magnetically launched wind

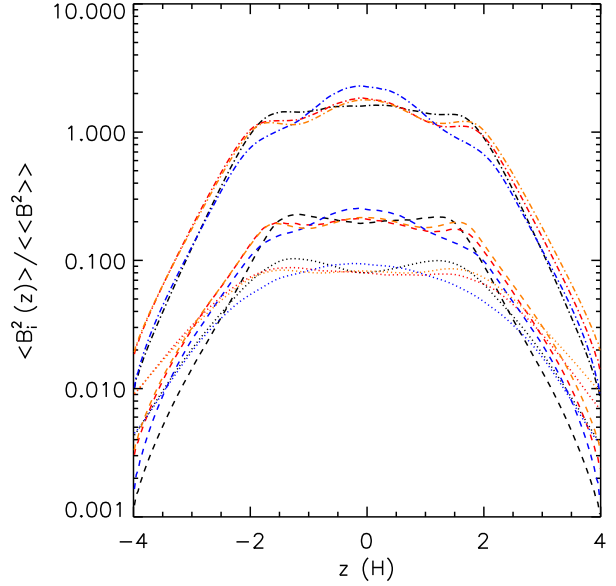


Figure 5. The time- and horizontally-averaged vertical profile of the magnetic field strength in individual components, $\langle B_i^2 \rangle$ ($i = x, y, z$), normalized to the volume integrated total magnetic energy strength, $\langle\langle B^2 \rangle\rangle$. These quantities are separately averaged. We omit data from the smallest domain (FT0.5) for the purposes of clarity. The black curve is from FT2, red is FT4, blue is FT8, and orange is Y16. As with Figure 4, the vertical structure of these quantities are consistent between all calculations: the energy density in toroidal fields dominates throughout the domain. In the region $|z| \lesssim 2H$, the ratio of energy densities is 4 : 40 : 1 ($x : y : z$), while in the region $|z| \gtrsim 3H$, the energy density in vertical fields exceeds that in radial fields, becoming comparable to (but still smaller than) the energy density in toroidal fields.

(e.g. Blandford & Payne 1982). Repeating run Y16 with an extended vertical domain (i.e. a domain size $16H \times 32H \times 16H$) could therefore yield insight into the launching of a magnetically driven wind from a turbulent accretion disc. The computational cost of such a simulation means that it is beyond the scope of the present work.

4 MESOSCALE SPATIAL CORRELATIONS

4.1 Magnetic Field

To examine the structure of the turbulence in the (x, y) plane, we employ the autocorrelation function (ACF) (see Guan et al. 2009), defined as,

$$\text{ACF}(f(\Delta\mathbf{x})) \equiv \left\langle \frac{\int f(t, \mathbf{x}) f(t, \mathbf{x} + \Delta\mathbf{x}) d^3\mathbf{x}}{\int f(t, \mathbf{x})^2 d^3\mathbf{x}} \right\rangle, \quad (8)$$

where f is the fluid quantity of interest, and the brackets denote a time-average. Note that we have defined the ACF to be normalized by its maximum value (at $\Delta x = \Delta y = \Delta z = 0$), and unlike Guan et al. (2009), we do not subtract off any mean quantities before calculating the ACF. Furthermore, for vector quantities, such as the magnetic field, we take the ACF of each component and then sum them as was done in Guan et al. (2009); $\text{ACF}(B) = \text{ACF}(B_x) + \text{ACF}(B_y) + \text{ACF}(B_z)$. The time average is done from orbit 50 to 125 in all cases.

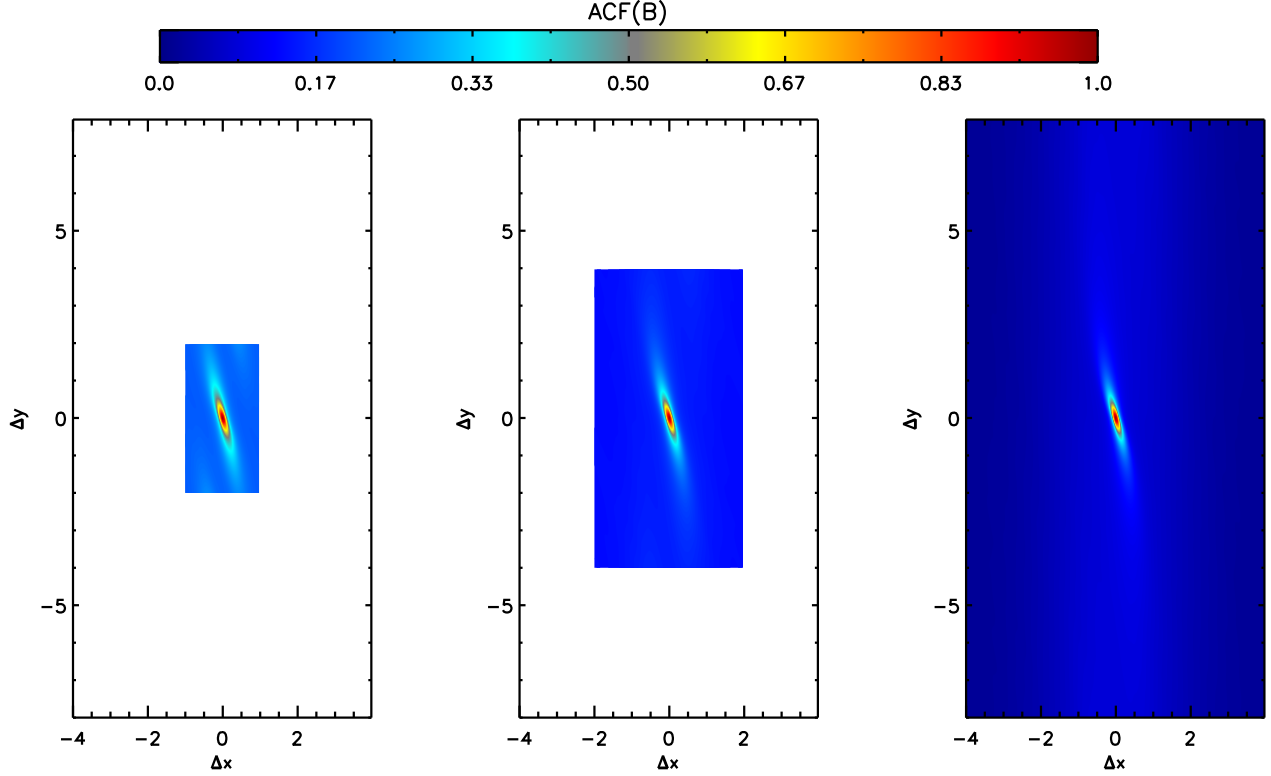


Figure 6. The ACF of the magnetic field, as defined by equation (8) and calculated for $|z| \leq 2H$, for FT2 (left), FT4 (middle), and FT8 (right) in the $\Delta z = 0$ plane. The tilted centroid structure of the magnetic field is the same size and shape in all three domains.

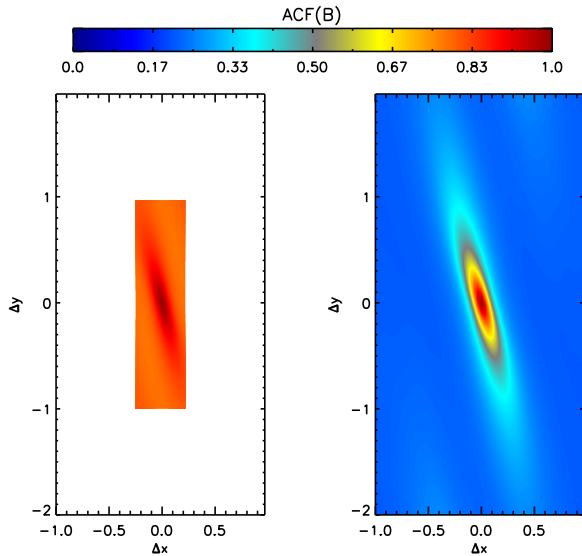


Figure 7. The ACF of the magnetic field, as defined by equation (8) and calculated for $|z| \leq 2H$, for the smallest domain (FT0.5, left) and the next largest domain (FT2, right) in the $\Delta z = 0$ plane. While the tilted centroid structure of the magnetic field appears to be mostly contained within the larger box, it is most definitely not contained in the smaller domain.

Because of the change in vertical structure at $|z| \sim 2H$, we have created two sets of ACFs, one for which we restricted the calculation to $|z| \leq 2H$, the other of which is for $|z| > 2H$. This will allow us to probe what has been referred to as the turbulent “disc region” ($|z| \lesssim 2H$) separately from the “coronal region” ($|z| \gtrsim 2H$). First focusing on the disc region, Fig. 6 shows the ACF of the magnetic field at $\Delta z = 0$ for the runs FT2, FT4, and FT8. To account for the large change in scale, we plot the same quantity for the two smallest domains, FT0.5 and FT2, in Fig. 7.

As in the vertical structure plots, there is a striking difference between the smallest domain and the larger ones. Although for the larger domains, the ACF has a small but nonzero value over extended regions (a point that we shall return to shortly), it is obvious that the tilted and elongated *centroid* of the ACF is well contained within the domain. This is not the case for FT0.5; indeed, it appears that the correlation length of \mathbf{B} extends beyond the size of the region, and that the peak of the centroid is not too much larger than the value of the ACF away from the centroid. Since α_{mag} is proportional to the “tilt angle” away from the y axis (Guan et al. 2009), the low average value of α_{mag} along with the extended ACF imply that transport of angular momentum by magnetic fields is reliant on the action of strong coherent toroidal magnetic fields, rather than small-scale turbulent structures.

Beyond the smallest domain, there generally appears to be two components to the ACF, one of which is strongly localized and tilted and which does not change significantly with domain size. The other component is more uniformly

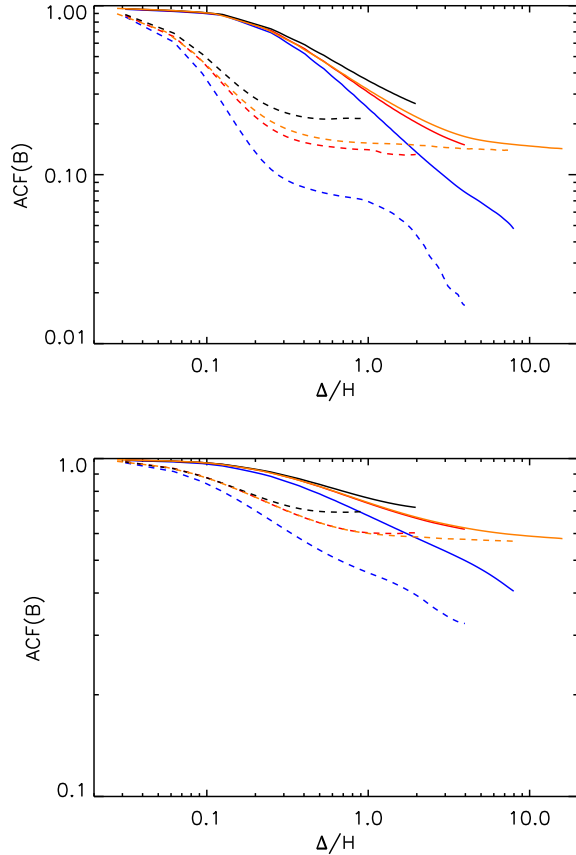


Figure 8. The ACF defined by equation (8) for the magnetic field taken along the major (solid lines) and minor (dashed lines) axes of the centroid. The top plot is $ACF(B)$ calculated for $|z| \leq 2H$, whereas the bottom plot is the same quantity but for $|z| > 2H$. We omit data from the smallest domain (FT0.5) for the purposes of clarity. The black curve is from FT2, red is FT4, blue is FT8, and orange is Y16. The magnetic field in the coronal regions has a larger correlation length than that within $2H$ of the mid-plane. In all cases, the magnetic field have a strongly localized component as well as a non-zero extended component that fills the simulation volume.

distributed in $(\Delta x, \Delta y)$ space and represents the background magnetic field. This component fills the entire domain, and in that sense cannot converge with increasing domain size. That is, as one makes the shearing box larger and larger, there is magnetic field that is always volume-filling, and thus there is always a component to the field structure that is correlated on the largest scales of the box.

To demonstrate this more quantitatively, Fig. 8 shows 1D slices of the ACF along the major and minor axes of the tilted structure. These plots include the largest box (Y16), but exclude the smallest domain size. The lower plot corresponds to $ACF(B)$ calculated in the coronal region. The ACF calculation in this region was done for $z > 2H$ and $z < -2H$ separately, and the resulting ACFs were averaged together. These plots again demonstrate that there are two components to the ACF, one that is concentrated and tilted, the other of which is uniform and extended. The tilted correlation structures are significantly larger in the coronal region compared to the disc region; the magnetic field has a larger correla-

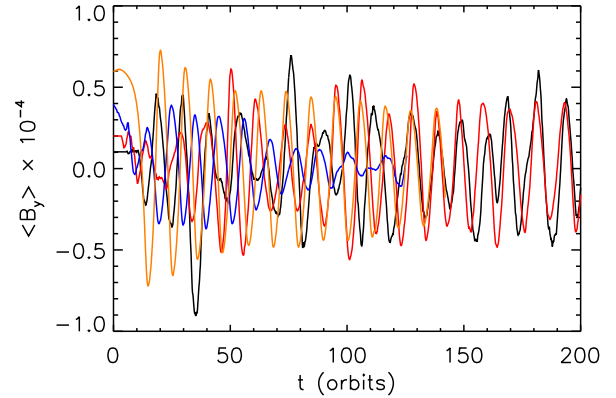


Figure 9. Time evolution of the volume averaged toroidal field (for all x, y and for $|z| \leq 2H$) in code units. FT2 is represented by the black curve, FT4 is the red curve, FT8 is the blue curve, and Y16 is the orange curve. All simulations show the oscillation of the mean toroidal field, but the oscillation amplitude is lower in FT8.

tion length in the coronal region. Furthermore, the value of the ACF for the extended component is larger than the corresponding component in the disc region. These observations suggest that the mean background field becomes a greater fraction of the magnetic energy in the coronal region (this is consistent with the two-dimensional correlation functions of Guan & Gammie 2011) and that the MRI modes that do operate in these regions produce fluctuations of relatively large length scale. This latter point is likely a result of the characteristic MRI wavelength becoming larger as the density drops (i.e., the Alfvén speed increases) in the corona.

Beyond comparing the coronal vs. disc regions, it is worth noting the convergence properties of the ACF as the domain size is increased. In both the coronal and disc regions, the inner centroid appears to be convergent with domain size. While the different ACFs at large Δ/H do not lie on top of each other, they are reasonably consistent with each other, with the exception of FT8 (the blue curve). In both the corona and disc regions, the extended ACF of FT8 appears significantly lower than the other domain sizes. We have examined the evolution of a volume-averaged $\langle B_y \rangle$ for these calculations (shown in Fig. 9); the FT8 run shows smaller amplitude (though still regular) variations in $\langle B_y \rangle$, resulting in a smaller background field component relative to small scale turbulent structures. The smaller background field relative to the turbulent fluctuations would certainly account for the lower extended ACF for FT8. We are not entirely sure why the background field is weaker in FT8 in the first place, though some statistical variation is to be expected since the evolution of $\langle B_y \rangle$ is modulated on rather long timescales (Simon et al. 2011).

To summarize, the horizontal structure of the magnetic field consists of an inner centroid that is tilted with respect to the azimuthal direction, as well as an extended component, likely due to the background magnetic field. The general shape of the ACFs converge, though as domain size is increased, there will always be structure at the largest scales of the box. These results have consequences for the physics of

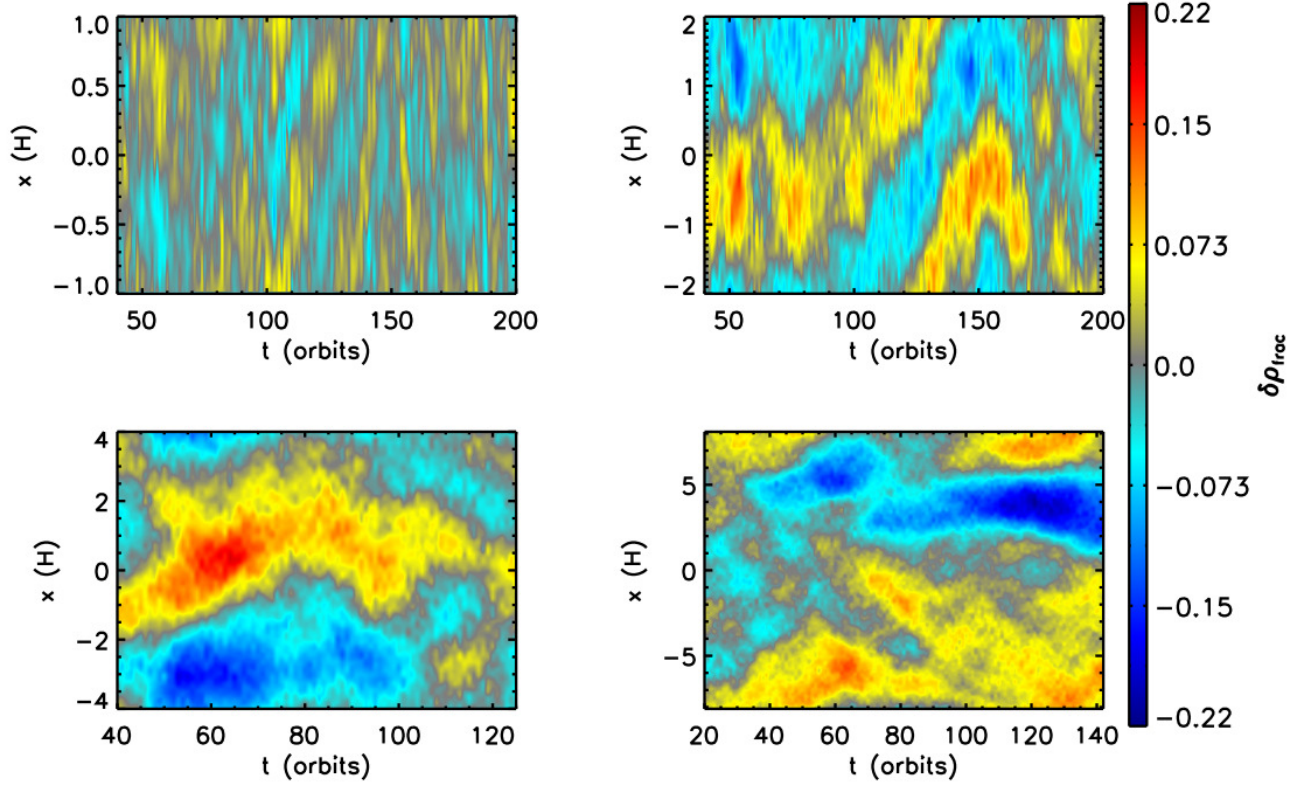


Figure 10. Space-time diagram of fractional gas density fluctuations, $\delta\rho_{\text{frac}}$ (as defined in the text) in the (t, x) plane. Note the different scales on both axes in each plot. For FT4 (upper right), and FT8 (lower left), there exists a $k_x L_x / (2\pi) = 1$ mode zonal flow. The zonal flow in Y16 (lower right) has a structure more complex than a simple $k_x L_x / (2\pi) = 1$ mode.

angular momentum transport in magnetized accretion discs, which we discuss in detail in §4.3.

4.2 Zonal Flows

We now turn to the structure and evolution of the gas density in the simulated discs. We are particularly interested in the existence and properties of zonal flows, long lived axisymmetric perturbations to the gas density that result from a geostrophic balance between pressure and Coriolis forces. Johansen et al. (2009) identified such flows in simulations of MRI disc turbulence, and suggested that they occur as a result of an inverse cascade in magnetic energy, which induces regions of super- and sub-Keplerian velocities. In broad terms, zonal flows are of physical interest because their existence within protoplanetary discs would provide a way to trap solid particles that are partially coupled to the gas disc through aerodynamic forces. Here, following prior work by Johansen et al. (2009) and Yang et al. (2011), we study whether the size and scale of the zonal flows converges with domain size.

Fig. 10 shows space-time diagrams in the (t, x) plane of the fractional perturbation $\delta\rho_{\text{frac}}$ to the density. In calculating $\delta\rho_{\text{frac}}$, we average the density over y and z , and then subtract off and normalize by the volume averaged ρ at each time. Note the change in both horizontal and vertical scale in each panel of the figure. For FT2 (upper left), there is essentially no indication of a zonal flow, but for the larger boxes, there

are large scale long-lived features in ρ . For FT4 and FT8, these features always fill the largest radial scale in the box (i.e., a $k_x L_x / (2\pi) = 1$ mode). The same diagram for the largest box (lower right), however, shows a structure more complex than a simple $k_x L_x / (2\pi) = 1$ mode.

To quantify the density structure further, we examine the ACF of ρ in the $(\Delta x, \Delta y)$ plane (the same averaging is done here as for ACF(B)). For simplicity, we only calculate the ACF over $|z| \leq 2H$. The result for FT2, FT4, and FT8 is shown in Fig. 11, and the ACFs for FT8 and Y16 are shown in Fig. 12. Note the range in ACF values from the color bar; in general, the density is very nearly uniform in the horizontal plane. However, in all domain sizes, there is a tilted and concentrated structure resembling the magnetic field ACF. This particular structure was also seen in the calculations of Guan et al. (2009). As domain size is increased, an axisymmetric structure appears. This structure, which appears to be more or less converged between the two largest runs, is due to the presence of zonal flows. We have also examined a one-dimensional slice along $\Delta y = 0$, shown in Fig. 13. The evidence for convergence is less persuasive in this one-dimensional slice than in Fig. 12, and the most that we can conclude is that there are tentative signs that the outer radial scale of the zonal flow is $\Delta x \sim 6H$ (implying a zonal flow wavelength of $\sim 12H$) and is contained within the largest spatial domain modeled. Running an even larger domain simulation could potentially nail down this radial scale. However,

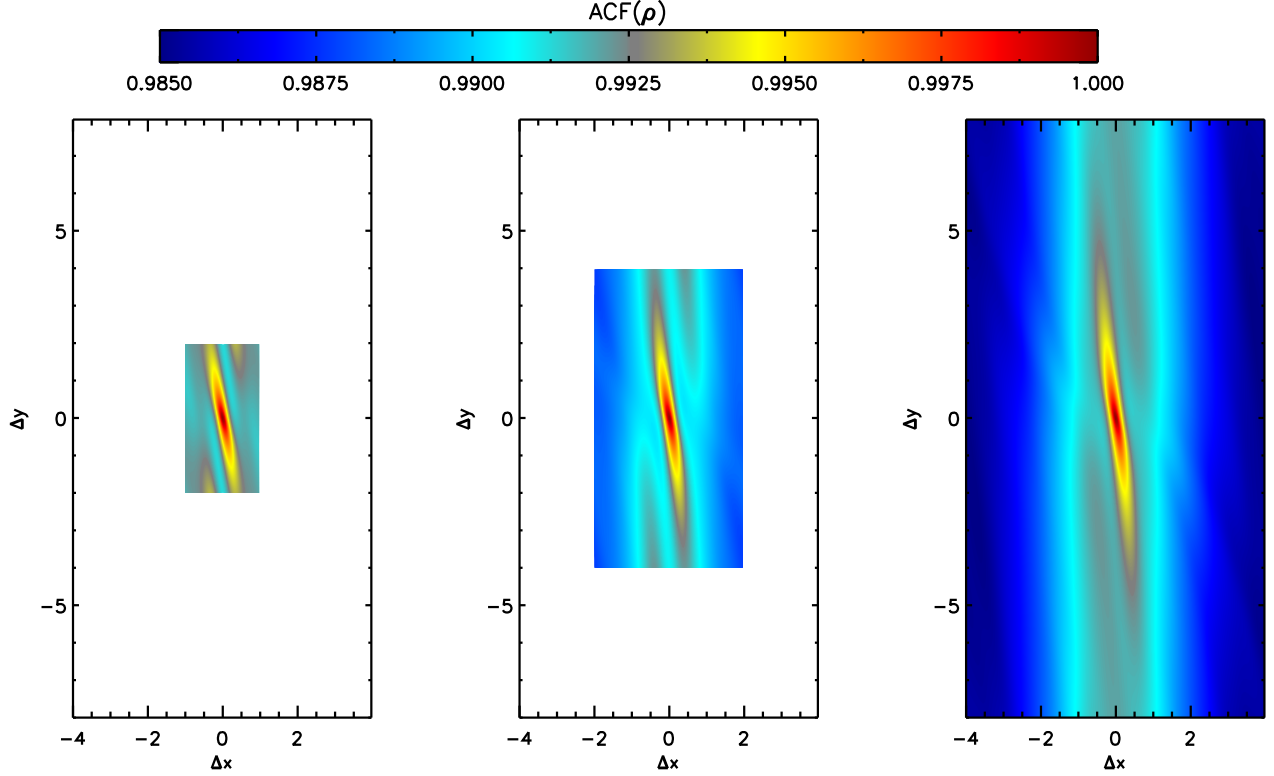


Figure 11. The ACF of the gas density as defined by equation (8) for FT2 (left), FT4 (middle), and FT8 (right) in the $\Delta z = 0$ plane. In all three ACFs, there is a tilted centroid structure. However, as domain size is increased, a larger scale axisymmetric structure appears.

such large domains become prohibitively computationally expensive given our current resources.

Finally, to explore whether the existence of zonal flows is sensitive to the initial conditions, we ran two additional simulations. They are the equivalent of FT4 but initialized with two flux tubes in one case, and with a uniform toroidal field (at constant β) in the second case. In both cases, a $k_x L_x / (2\pi) = 1$ mode zonal flow appears around 10-20 orbits into the simulations.

4.3 Locality of Angular Momentum Transport

In the preceding sections, we have demonstrated that there are mesoscale correlations within the turbulent disc ($|z| < 2H$) in both the magnetic field and the density. The existence of such structures can have important consequences for the physics of angular momentum transport in magnetized accretion discs. For example, if the mesoscale correlations in the magnetic field within the turbulent disc discussed in §4.1 are actively generated from the magnetorotational instability, then these fields can also transport angular momentum through the Maxwell stress term in the angular momentum conservation equation (Balbus & Papaloizou 1999). Similarly, the zonal flows discussed in §4.2 are associated with sub- and super-Keplerian velocities which form due to the action of magnetic forces (Johansen et al. 2009); such flows can then be associated with transport of angular momentum as they drift through the disc. In both of these cases, we would expect to measure angular momentum transport (through the

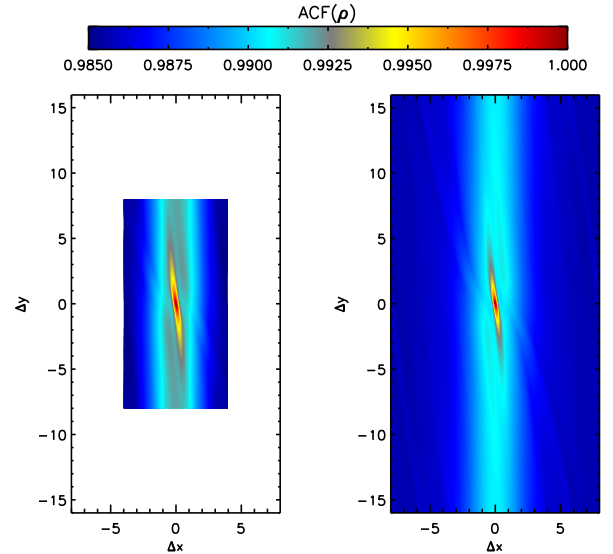


Figure 12. The ACF of the gas density as defined by equation (8) for FT8 (left) and Y16 (right) in the $\Delta z = 0$ plane. The density structure is consistent between these two domain sizes, including the large scale axisymmetric component.

Maxwell and Reynolds stress, respectively) on scales $\gg H$. Such a result would undercut the assumption that angular

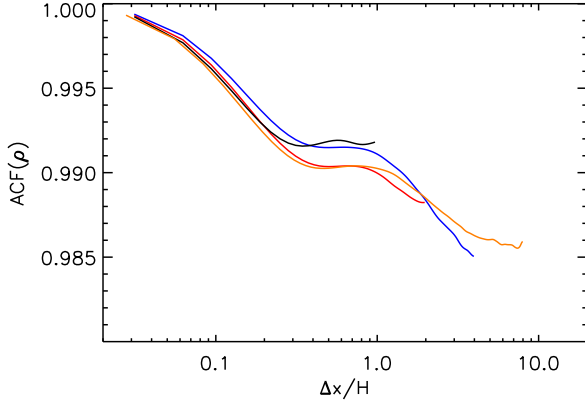


Figure 13. The ACF of the gas density as defined by equation (8) versus Δx along $\Delta y = 0$ and $\Delta z = 0$. The colors denote the various runs; black is FT2, red is FT4, blue is FT8, and orange is Y16. All ACFs show a central component that flattens out at $\sim 0.3H$. For boxes larger than FT2, there is a second dip corresponding to the presence of a zonal flow. Finally, there is hint of this second dip flattening out for Y16, thus providing tentative evidence for an outer scale to the zonal flow that is contained within the simulation domain.

momentum transport in magnetized discs can be treated as a purely local process (Shakura & Sunyaev 1973).

We can test these ideas by examining the ACF for the Maxwell and Reynolds stress. If angular momentum transport within the disc is determined locally, we would expect the ACF of the stress to decay rapidly on scales $\gtrsim H$; correlations on scales $\gg H$ would indicate a *non-local* component to angular momentum transport (Gammie 1998). Figure 14 plots one-dimensional slices along the major and minor axes of the tilted centroid component of the ACF for the Maxwell stress, $\text{ACF}(-B_x B_y)$ (top panel), and Reynolds stress, $\text{ACF}(\rho v_x \delta v_y)$ (bottom panel), calculated over the region $|z| \leq 2H$, i.e. within the “turbulent disc”. The data of this figure demonstrate that while the ACFs are strongly concentrated within $\lesssim H$, there is an extended component, correlated at $\sim 20\%$ for the Maxwell stress and $\sim 8\%$ for the Reynolds stress, that fills the simulation domain. Essentially, these results imply that there is a net background Maxwell and Reynolds stress resulting from mesoscale structures in the magnetic field and density, on top of which turbulent stress fluctuations are imposed.

To verify this result, we (for all runs except FT0.5) examined the time-averaged (from orbit 50 onward) vertical profile of the quantity

$$\frac{-\langle B_x \rangle \langle B_y \rangle}{\langle -B_x B_y \rangle}, \quad (9)$$

which represents the fraction of the average Maxwell stress that resides in the large scale background magnetic field. We find that this ratio is quite small near the disk mid-plane but increases dramatically away from the mid-plane, leveling out to $\sim 0.3-0.4$ for $|z| \gtrsim 2H$. The conclusion from these calculations is clear: while angular momentum transport within magnetized accretion discs is highly localized, there is, in addition, a significant *non-local* component, the existence of which

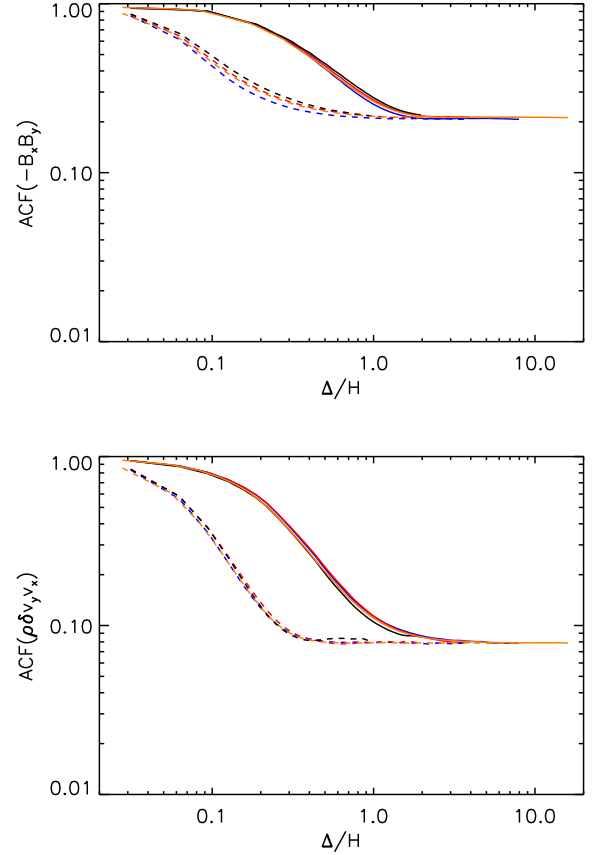


Figure 14. As in the top panel of Figure 8 for the ACF of the Maxwell (top panel) and Reynolds (bottom panel) stress. While the ACFs are strongly concentrated within $\lesssim H$ of the centroid, there is an extended component, correlated at $\sim 20\%$ for the Maxwell stress and $\sim 8\%$ for the Reynolds stress, that fills the simulation domain in all cases.

implies that models founded upon a purely local description of angular momentum transport are incomplete.

The origin of these mesoscale correlations in the Maxwell stress can be understood, at least in part, by considering the saturation characteristics given in Table 2. In all of the simulations, the turbulent disc is dominated by strong toroidal magnetic fields (making up $\sim 80\%$ of the magnetic energy in simulation Y16). The toroidal field MRI is well-resolved according to the criteria of Sano et al. (2004), which specifies the number of zones per characteristic wavelength of the instability. In principle, all modes with wavelengths *longer* than this characteristic wavelength are unstable. This is in contrast to the case of the vertical field MRI, where wavelengths longer than that of the pressure scale height are expected to be stabilized. Thus, it is not unexpected that long wavelength structures form in the turbulence from the toroidal field MRI. We discuss this further in Section 7.

5 TEMPORAL VARIABILITY

We now return to the behaviour of the temporal variability in domains of different size. From Fig. 2, it is clear that there is

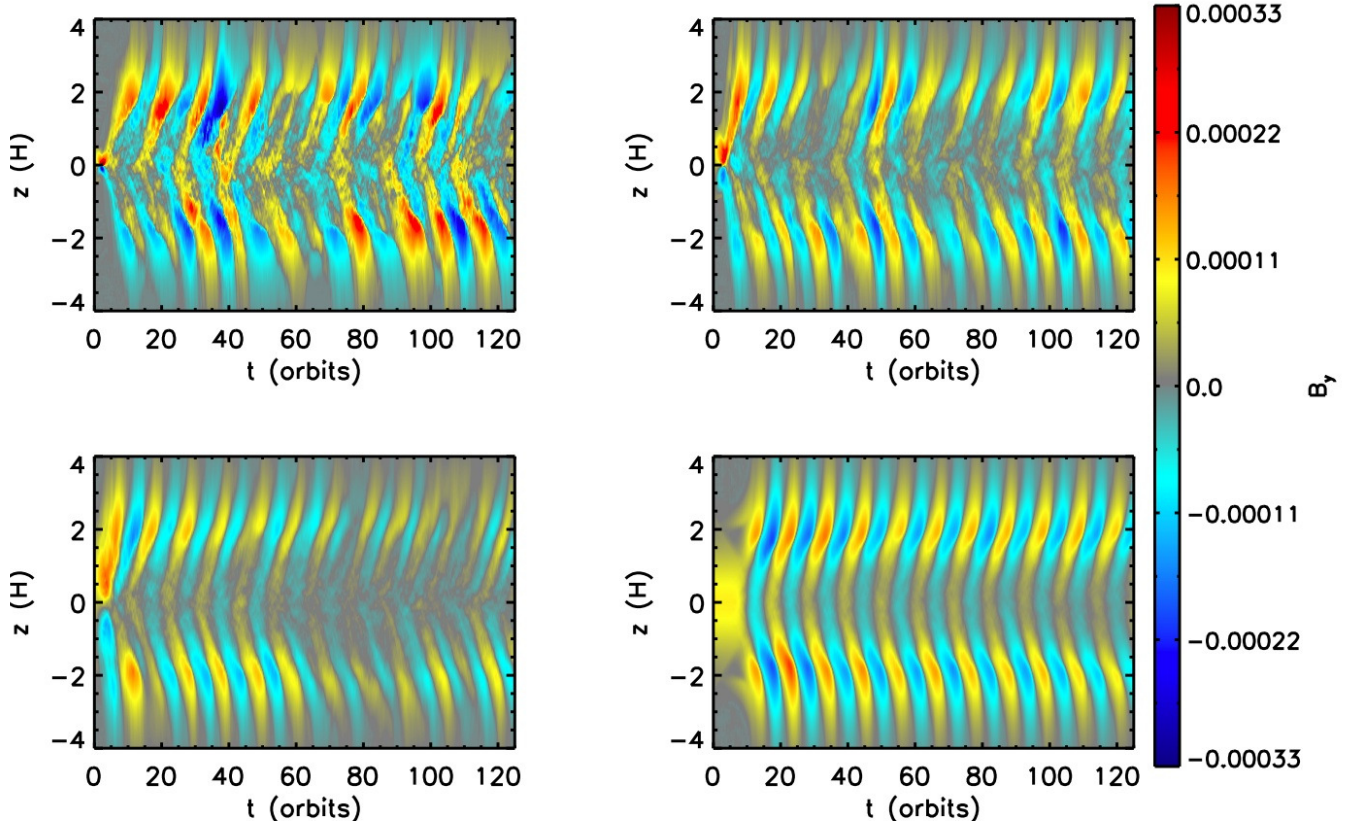


Figure 15. Space-time diagram in (t, z) for the horizontally averaged B_y in FT2 (upper left), FT4 (upper right), FT8 (lower left), and Y16 (lower right). The so-called "butterfly diagram" present in vertically stratified MRI-driven discs is apparent in all four domain sizes, and becomes more regular as the domain size is increased.

a marked decrease in temporal variability as the domain size is increased. This is generically true for a variety of quantities. Figure 15, for example, shows the (t, z) space-time diagram of B_y for the four largest domain sizes. The dominant feature in this diagram is the ~ 10 orbital period flipping of B_y that has been observed in many previous calculations (e.g., [Brandenburg et al. 1995](#); [Davis et al. 2010](#); [Simon et al. 2011](#); [Guan & Gammie 2011](#)). However, superimposed upon this is a stochastic component to B_y , which becomes smaller as the domain size is increased.

To better quantify this behavior, we define a diagnostic, which represents the fractional power in temporal fluctuations,

$$P_{\text{var}} \equiv \frac{\text{Var}[\langle f \rangle]}{\text{Avg}[\langle f \rangle]^2}. \quad (10)$$

Here, "Var" refers to the temporal variance of the quantity of interest, and "Avg" is the temporal average of the quantity. Figure 16 shows this quantity versus box size for both the total stress (squares) and the magnetic energy (asterisks), calculated from orbit 50 onward within the "turbulent" disc ($|z| < 2H$). The data of this figure demonstrate that there is a clear decrease in the variability with increasing domain size. Specifically, as we increase the domain size from $2H \times 4H \times 8H$ (FT2) to $8H \times 16H \times 8H$ (FT8) (a factor 16 increase in volume), we find that the fractional variability decreases by approximately a factor 10. Increasing the volume by a further factor of four (i.e. from simulation FT8 to Y16)

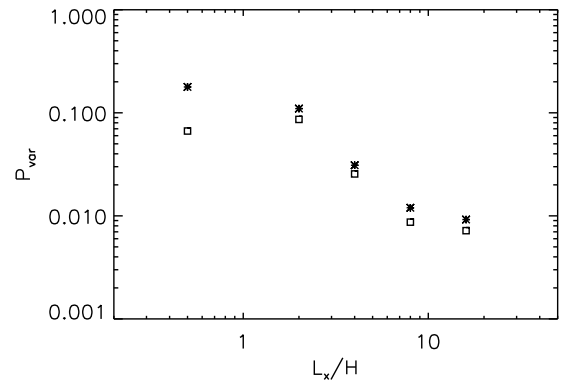


Figure 16. Variability of the volume-averaged stress (squares) and magnetic energy (asterisks), as defined by P_{var} (equation 10) and averaged over all x and y and for $|z| < 2H$, versus box size. As the domain size is increased, the average temporal variability decreases.

results in only a (comparatively) small decrease in fractional variability, suggesting that we are approaching convergence at this largest domain size.

One might expect that the volume averaged variability will decrease as domain size is increased; as we average over increasing numbers of (largely) uncorrelated subvolumes, the fractional variability of the system will decrease. If this sta-

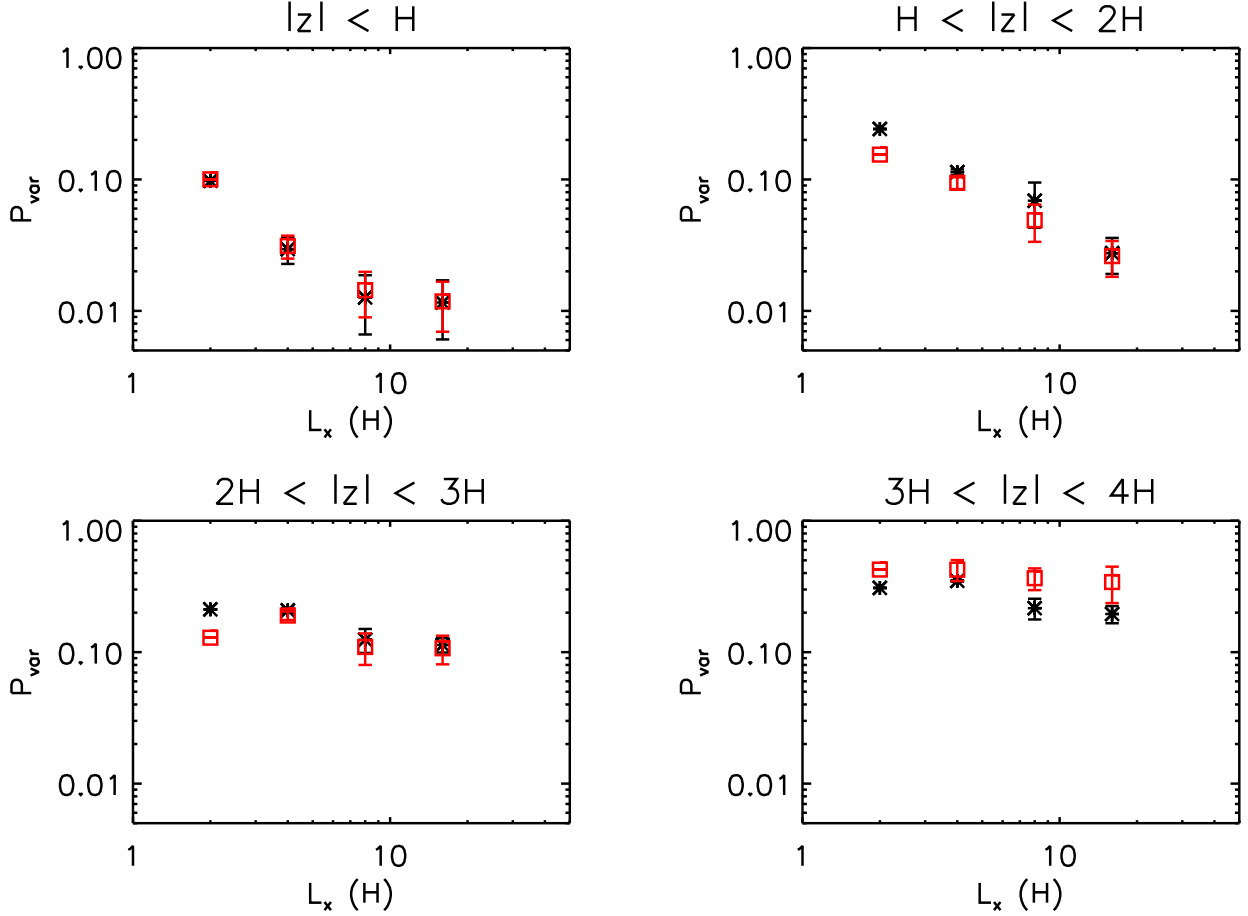


Figure 17. Variability of the stress (red squares) and magnetic energy (black asterisks) as defined by P_{var} (equation 12) versus box size. This is the same quantity as is plotted in Fig. 16. However, the total domain is broken into horizontal subdomains of size $2H \times 4H$, after which P_{var} is calculated for that subdomain. All values of P_{var} are then averaged together and plotted against the box size. The error bars denote one standard deviation about the average over subdomains. As labelled, each panel corresponds to a different vertical region in the shearing box. The primary result of this figure is that near the mid-plane, temporal variability decreases uniformly throughout the grid as domain size is increased, whereas for $|z| \gtrsim 2H$, this variability is constant with domain size.

tistical effect is solely responsible for the observed decrease in variability, we would expect the variability associated with a small domain within the simulation volume to remain unchanged as the volume is increased. To test this notion, we divide each shearing box into horizontal subdomains of size $L_x \times L_y = 2H \times 4H$ (i.e. the domain size of simulation FT2 on the $x - y$ plane), calculate P_{var} in each subdomain, and then average the P_{var} . This quantity is plotted in Fig. 17 for a variety of vertical regions in each shearing box, excluding the smallest, FT0.5. The error bars denote one standard deviation about the average P_{var} value. Thus, the error bars do not represent temporal variability but instead quantifies the spread in P_{var} values between the subdomains.

In the corona $|z| \gtrsim 2H$, the variability of the subdomains remains constant as domain size increases, but in the turbulent disc ($|z| \lesssim 2H$), the variability of the subdomains decreases with increasing domain size. As the shearing boxes are increased in size, the *physics* of the turbulence changes such that variability within the turbulent disc ($|z| \lesssim 2H$) decreases everywhere uniformly, while the variability in the coronal region remains constant.

6 COMPARING THE MESOSCALE AND GLOBAL REGIMES

Measured in units of H , our largest shearing boxes span radial extents that are not so different from those modeled in some global calculations. It is therefore possible to directly compare some of our results to those obtained from studies of disc turbulence in the global regime. We restrict our comparison to recent global simulations which attain comparable resolutions to the 32 zones per H of the local runs (such as Beckwith et al. 2011; Sorathia et al. 2011). The most secure comparisons are probably with the simulations of Sorathia et al. (2011); these have orbital advection implemented, which leads to a significant reduction in numerical diffusion. We note that quantitative comparisons are not always possible: there are significant and unavoidable differences in the setup and analysis between the local and global runs. We also note that the scale height defined in Beckwith et al. (2011) and Flock et al. (2011a) is a factor of $\sqrt{2}$ smaller than the scale height defined here. While this is an order unity

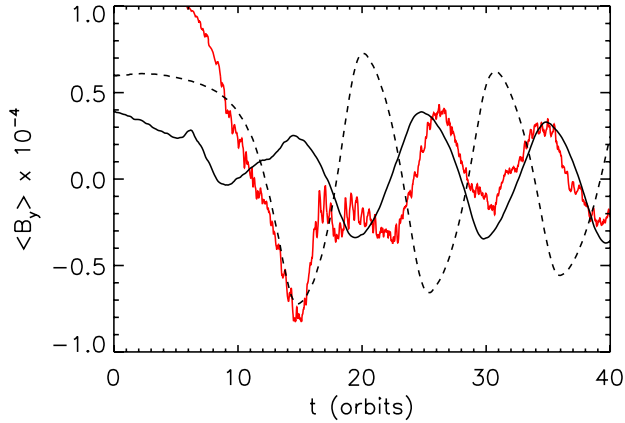


Figure 18. Time evolution of the volume averaged toroidal field in code units (for all x, y and for $|z| \leq 2H$). The solid black curve is FT8, the dashed curve is Y16, and the red curve is global simulation data from Beckwith et al. (2011) (their Fig. 3), renormalized to match the vertical scale of the shearing box data and plotted against the time unit of the local simulations. The early evolution of the net toroidal flux is comparable between the global and local simulations; the initial net flux is rapidly expelled after which the flux oscillates about zero. The original global simulation data from Beckwith et al. (2011) is for 20 orbits at 15 Schwarzschild radii. The agreement between the curves in the figure suggest that the dynamo present in the simulation of Beckwith et al. (2011) has a characteristic radius of 10 Schwarzschild radii, at which the duration of each cycle of the dynamo is 10 orbits and agrees with local simulations.

effect, it should be borne in mind when making direct comparisons between that work and the work presented here.

To start, we consider the standard α and α_{mag} parameters. In all of our calculations, we find that $\alpha \sim 0.02 - 0.03$, not significantly different than the same parameter calculated (albeit calculated differently) in global simulations. Figure 5 of Beckwith et al. (2011) displays α versus time. While there is a long term decrease in the α value, their values range from 0.02 to 0.06. The results of Flock et al. (2011a) give $\alpha \sim 0.005 - 0.02$, somewhat lower than our values and the Beckwith et al. (2011) values. Sorathia et al. (2011) calculated α for various initial field geometries; they find that α ranges from ~ 0.01 to ~ 0.08 depending on the field geometry and resolution.

Again considering Fig. 5 of Beckwith et al. (2011), the dashed lines in the bottom panel show α_{mag} as a function of time, which is relatively constant after the initial growth of the MRI. The values of α_{mag} range between 0.3 and 0.4, generally consistent with all of our runs (except for FT0.5 as elaborated upon above), for which $\alpha_{\text{mag}} \sim 0.4$. The highest resolved global simulations in Hawley et al. (2011) have $\alpha_{\text{mag}} \sim 0.2 - 0.4$, again generally consistent with our shearing box results (though, somewhat lower). This quantity can be related to the tilt angle of the magnetic correlation function (Guan et al. 2009; Sorathia et al. 2011), which is what Sorathia et al. (2011) focused on calculating. Our typical value of $\alpha_{\text{mag}} \sim 0.4$ corresponds to $\theta_{\text{tilt}} \sim 12^\circ$ in general agreement with the Sorathia et al. (2011) calculations. The global calculations of Flock et al. (2011a) return $\theta_{\text{tilt}} \sim 8 - 9^\circ$, slightly lower than our value as well as that of Sorathia et al. (2011).

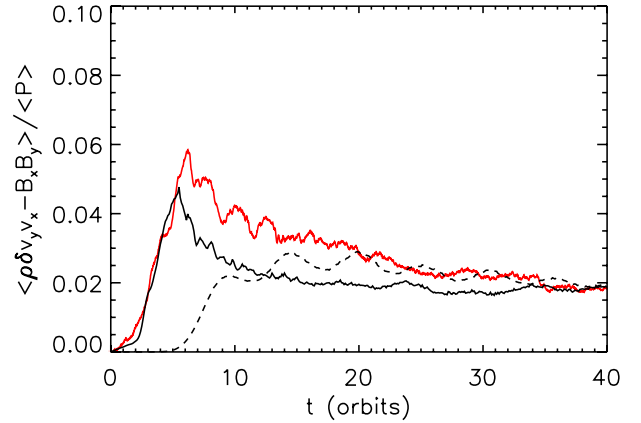


Figure 19. Volume averaged stress normalized by the volume averaged gas pressure versus time for FT8 (black solid line), and Y16 (dashed line). This average was done over all x and y and for $|z| \leq H$. The red curve is the equivalent normalized stress from Beckwith et al. (2011). The horizontal scale is chosen to match that of Fig. 18, and as such, the global data is more representative of a radius of 10 Schwarzschild radii, as explained in the text and Fig. 18. Similar variability levels are observed in both local simulations and global simulations.

Other behaviors are best compared in a more qualitative manner. The “butterfly diagram” appears to be a robust feature of vertically stratified MRI-driven turbulence. It has been seen in several global calculations (e.g., O’Neill et al. 2011; Beckwith et al. 2011; Flock et al. 2011b,a), and the period of the azimuthal field sign flipping is approximately 10 local orbits with power shared radially (O’Neill et al. 2011). Looking again at the time histories of the pressure-normalized total stress in global simulations, the temporal variability in the global simulations appear to be quite small (Beckwith et al. 2011; Flock et al. 2011a), similar to the largest shearing boxes presented here. A more explicit comparison can be made by examining the history of the largest shearing boxes presented here over the duration of a well-resolved global simulation. To do so, we note that Fig. 3 of Beckwith et al. (2011) plots the time-history of the toroidal magnetic flux within the simulation domain, which exhibits transient behaviour, followed by two complete dynamo cycles. In Fig. 18, we combine this global simulation data with the history of simulation FT8 and Y16. Note that the local data is plotted over 40 orbital periods, whereas the data presented by Beckwith et al. (2011) is for 20 orbits at 15 Schwarzschild radii. This would suggest that the dynamo present in the simulation presented in Beckwith et al. (2011) has a characteristic radius of 10 Schwarzschild radii, at which the duration of each cycle of the dynamo is 10 orbits. The figure shows a comparable evolution between the local and global simulations; transient behavior (corresponding to expulsion of toroidal flux from the simulation domain) lasts for ~ 15 orbits, after which the MRI dynamo produces toroidal magnetic fields of alternating sign on a 10 orbit timescale. Figure 19 shows the stress evolution comparison over this same time period for FT8 and Y16 averaged over all x and y and for $|z| \leq H$. A more direct comparison will be necessary in the future (e.g., calculating the P_{var} parameter

in a shearing box sized region of a global simulation), but this basic comparison suggests that our largest boxes are reaching the temporal variability level seen in global simulations.

The vertical structure of the turbulence, namely the magnetic field, is another point of comparison. Our calculations show a roughly flat distribution of the gas pressure normalized stress at ~ 0.01 for $|z| \lesssim 2H$, after which the stress drops to $\sim 10^{-4}$ (see Fig. 4). The same figure shows that β peaks near 40 and then drops below unity outside of $|z| = 2H$. In Beckwith et al. (2011), the normalized stress peaks near ~ 0.01 and $\beta \sim 30$ at its peak, generally consistent with our results. However, the behavior away from the mid-plane differs dramatically from what is seen in our local calculations. In particular, the stress does not drop nearly as rapidly outside of $|z| = 2H$, and β never drops below unity. This difference in behaviors away from the mid-plane could be due to the use of periodic boundary conditions in the global simulations of Beckwith et al. (2011). The general structure of β in the global BO model of Flock et al. (2011b), which has vertical outflow boundary conditions, (their Fig. 11) is similar to what we observe in our local calculations except that everything appears to be scaled up by a factor of ~ 10 in Flock et al. (2011b). That is, their peak β value is ~ 500 , and at $|z| \approx 2H$, $\beta \sim 10$. The reason for this large difference is not at all clear.

All of these comparisons, with the exception of the vertical magnetic structure, yield good agreement between local and global calculations, considering the spread in resolution and measurement techniques. However, the real question we have set out to answer in this paper is whether or not the mesoscale appears the same between these two calculations; this has yet to be addressed. The most relevant measure for answering this question is the correlation function of various turbulent structures in the horizontal plane.

The analysis of Beckwith et al. (2011) and Flock et al. (2011a), shows a tilted, highly localized component to turbulent fluctuations, in agreement with the results found in this work. In their analysis, Beckwith et al. (2011) subtract off large scale variations (due to radial and vertical gradients) to only focus on the central, tilted component. They then calculate a correlation length along the major and minor axes of the tilted structure by determining the length at which the correlation function drops by a factor of e^{-2} (see their Table 1). Flock et al. (2011a) calculates the same lengths but by using the half width at half maximum of the correlation function. The correlation length values between these two papers generally agree, though it should be noted that Beckwith et al. (2011) consider the ACF of the magnetic energy, whereas Flock et al. (2011a) calculate the ACF for \mathbf{B} as was done here and in Guan et al. (2009).

In our calculation of the ACF, we do not subtract off any background component. However, we can consider the correlation length along a given axis to be the point at which the ACF begins to flatten out. Beyond this length, the ACF is flat because the structure is relatively uniform; thus, the "knee" in the curve represents the outermost scale of the localized component to the ACF. From Fig. 8, it appears that the correlation lengths for \mathbf{B} are $\lambda_{B,\text{maj}} \sim 4 - 5H$ and $\lambda_{B,\text{min}} \sim 0.3 - 0.4H$. Viewing the equivalent plot for B^2 and ρ gives $\lambda_{B^2,\text{maj}} \sim 2 - 3H$, $\lambda_{B^2,\text{min}} \sim 0.2H$, and $\lambda_{\rho,\text{min}} \sim 0.3 - 0.4H$. We did not calculate a major axis correlation length for ρ because the

ACF never flattened out along the major axis. This is likely related to the presence of the axisymmetric zonal flows entering into the ACF calculation, though it is still not clear why the ACF does not flatten out at some point along the major axis. In any case, it would seem that there is rough agreement between the correlation length of the tilted, localized ACF component in global and local calculations.

The general agreement between these correlation lengths is very encouraging as it shows that MRI-driven turbulence has the same small scale structure in both local and global simulations. However, a primary result of the work here is that in addition to the tilted component of the magnetic field structure, there is also a non-negligible, volume filling background component. Again, since the large scale component was subtracted off in the analysis of Beckwith et al. (2011), a direct comparison with our results cannot be made very easily. However, some information can be extracted by examining their Fig. 4, which shows the structure of the toroidal magnetic field on the azimuthal plane. The figure shows that this field has structure in both the vertical and radial dimensions; there appear to be magnetic field bundles that evolve throughout the disc. Through a very rough examination of this figure, it appears that the radial size of these bundles is $\sim 5r_s$, where r_s is the Schwarzschild radius. In those calculations, $H/R = 0.07$ so that at $R = 10r_s$, $H = 0.7r_s$. Thus, the typical size of the magnetic field bundles in that figure is estimated to be $\sim 7H$ where (as noted above) this H is that defined in Beckwith et al. (2011), a factor of $\sqrt{2}$ smaller than the H that we use. This scale translates to $\sim 5H$ using H defined as we have in this paper, which should definitely be captured in our largest shearing box, Y16. However, the correlation function of \mathbf{B} clearly indicates that there is a volume-filling background component to the magnetic field; there is no structure associated with $\sim 5H$. Granted, this comparison is murky at best, and perhaps even larger shearing boxes would show the presence of such radial structure. However, these results suggest that there may be a fundamental difference in radial magnetic structure at the mesoscale between local and global simulations, perhaps a result of the inclusion of curvature terms in global simulations.

The presence of density zonal flows in global calculations done to-date is questionable at best. To our knowledge, the best evidence for such flows exist in the global calculations of Lyra et al. (2008); see their Fig. 10, which shows reasonably long-lived radial variations in the gas density. However, even here, the flows are only weakly detected and not discussed by the authors in any detail. It would thus seem that these flows are very difficult to detect in global calculations. This difficulty may result from larger scale density gradients dominating the weaker zonal flow variations. While our work here has shown tentative evidence for a converged outer scale to these flows in shearing boxes, it is still not clear whether or not such flows are an artifact of the shearing box approximation that tend to exist on the largest radial scales. Thus, we believe that the detection of these structures in global simulations should be a very important priority for future work, one that we are currently pursuing.

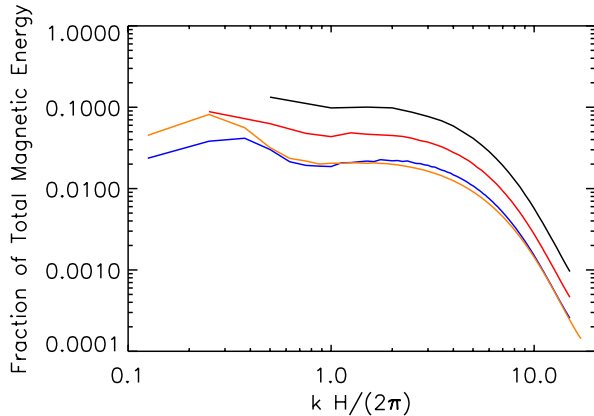


Figure 20. Fraction of the total magnetic energy as a function of isotropic wavenumber k . In calculating these curves, we averaged the three-dimensional Fourier transform of magnetic energy over spherical shells of constant k and then averaged the resulting one-dimensional power spectra in time, from orbit 50 to 125. We omit data from the smallest domain (FT0.5) for the purposes of clarity. The black curve is from FT2, red is FT4, blue is FT8, and orange is Y16. As domain size is increased, the fraction of the total magnetic energy at the smallest scales decreases while the largest fraction of magnetic energy resides at the largest scales. There appears to be convergence between the two largest domain sizes.

7 DISCUSSION, SUMMARY, AND CONCLUSION

We have examined the convergence properties of MRI-driven MHD turbulence with increasing domain size, i.e. as we transition from the “local” ($H \sim L \ll R$) to “mesoscale” ($H \ll L \ll R$) regime. We have found that volume-averaged quantities (such as the [Shakura & Sunyaev 1973](#), α -parameter and the ratio of the Maxwell stress to magnetic energy, α_{mag}) converge rapidly as we transition between these regimes. We have also studied the properties of the magnetic field autocorrelation function (ACF) as we move between these regimes, which reveals a two component structure to the magnetic field. One is highly localized and tilted with respect to the azimuthal direction, consistent with previous findings (e.g., [Guan et al. 2009](#)). The other component is extended to the largest scales in the domain, and is likely associated with the (predominantly toroidal) background magnetic field. Furthermore, we have identified the zonal flows of [Johansen et al. \(2009\)](#) in our domain sizes of scale $4H \times 8H \times 8H$ and larger. These flows always fill the largest radial scale in the box except for our largest simulation. We find tentative evidence that the radial wavelength of these flows converge at $\sim 12H$.

These results have important implications for the physics of angular momentum transport in magnetized accretion discs. While the ACFs of the Maxwell and Reynolds stress are strongly concentrated within $\lesssim H$, both of these quantities are also correlated on scales $\gg H$ at the $\sim 20\%$ and $\sim 8\%$ level respectively. If angular momentum transport in magnetized accretion discs is a purely local process, then the ACF of these quantities should drop to zero on scales $\sim H$ ([Gammie 1998](#)). That the ACFs of the accretion stress remain finite at scale $\gg H$ undercuts the assumption that angular momen-

tum transport in magnetized discs can be treated as a purely local process ([Shakura & Sunyaev 1973](#); [Pringle 1981](#)).

We have also found that the transition to the mesoscale limit is associated with a decrease in the temporal variability of the turbulent disc, an effect that is not solely due to volume-averaging over uncorrelated subdomains. It is perhaps not surprising that the small scale physics of MRI-driven turbulence changes with increasing box size; as larger magnetic structures are permitted in the box, large scales can potentially interact with smaller scales and change the variability properties at these scales. While a spectral energy transfer analysis ([Fromang & Papaloizou 2007](#); [Fromang et al. 2007](#); [Simon & Hawley 2009](#)) would be useful in understanding how exactly different scales interact, we can attain a basic understanding by considering the time-averaged power spectra of the magnetic energy, as shown in Fig. 20. In calculating this power spectra, we took a full three-dimensional Fourier transform, averaged the result over spherical shells of constant k , and then time averaged the resulting spectra from orbit 50-125. The figure shows the fraction of the total magnetic energy that exists at a scale k (i.e., integrating each curve over k would return unity). As box size is increased, the power spectra shift downwards because there are more spatial scales over which the magnetic energy can be distributed. However, the main point to take away from this figure is that as the box size is increased, the fraction of the total magnetic energy at the smallest scales generally decreases while the largest fraction of magnetic energy resides at the largest scales, with signs of convergence between the two largest domain sizes, (this result is consistent with Fig. 2 of [Johansen et al. 2009](#)). Since the turbulent energy levels are roughly the same between all of these simulations (e.g., Fig. 3), increasing the domain size equates to more power being taken from the small scales and put into the largest scales. How and why exactly this behavior occurs is still an open question. However, this result is consistent with our notion that the largest scales in the shearing box play a very important role in the evolution of the MRI.

We have also examined the physical properties of shearing boxes computed using restricted spatial dimensions, e.g. $0.5H \times 2H \times 8H$ in $L_x \times L_y \times L_z$. Turbulence arising from the MRI in these simulations is characterized by a greater level of isotropy ($\alpha_{\text{mag}} = 0.16$) than is found in larger shearing box domains (those with $L_x \geq 2H \times L_y \geq 4H$). Furthermore, we find anomalous structures in both the ACFs and vertical profiles of (e.g.) the magnetic energy. These results suggest that simulation domains of this size or smaller could produce misleading results. One such use of small domains (necessary for numerical reasons) is in radiation pressure dominated MRI simulations (e.g., [Hirose et al. 2009](#); [Blaes et al. 2011](#)). However, the ACF of the magnetic field in these simulations strongly resembles that of our converged FT2 calculation ([Hirose](#), private communication), despite the fact that the scale height of these radiation pressure dominated simulations is not very different from an isothermal disk scale height as we have in our calculations ([Krolik](#), private communication). This surprising result indicates that the thermodynamic properties of the disk may play a role in determining the detailed structure of MRI-driven turbulence.

We have compared results from the largest domain sizes considered here ($8H \times 16H \times 8H$ and $16H \times 32H \times 8H$) with those obtained from well-resolved global simulations

that have been recently presented in the literature (e.g., Beckwith et al. 2011; Sorathia et al. 2011). We have found broad agreement between these two classes of simulations, in terms of volume-averaged quantities, the vertical structure of and correlations lengths within the turbulence. A point of contention however, is the largest spatial scale on which (e.g.) the magnetic field is correlated. The mesoscale simulations presented here suggest that correlations exist on radial scales up to the maximum considered ($16H$). Crude analysis of the results of Beckwith et al. (2011) suggests, however, a maximum radial correlation length of $\sim 5H$. This result may indicate that the maximum radial correlation length of the magnetic field is determined by global (e.g., curvature), rather than local effects. Furthermore, if mesoscale structures in the magnetic field and accretion stress originate in the action of the toroidal field MRI, then global simulations that probe up to $m = 1$ in azimuth, utilizing resolutions equivalent to the simulations presented here, will be necessary to determine the outer scale of these quantities. Since there are non-negligible levels of angular momentum transport at the largest azimuthal scales, a first-principles global treatment of the system is necessary to understand the complete physics of angular momentum transport.

Overall, our results suggest several avenues of future work. If, as suggested by our results and those of Beckwith et al. (2011), a significant amount of angular momentum transport takes place on scales $\gg H$, it will be important to determine the length scale on which the work done by this large scale angular momentum transport is dissipated. Hirose & Turner (2011) suggest that the magnetic fields associated with this large scale angular momentum transport can rise buoyantly into the disc corona ($|z| > 2H$), where they can be dissipated. If this is the case, then the local connection between angular momentum transport and disc heating would be broken, further undermining the assumptions of local models of angular momentum transport (Balbus & Papaloizou 1999). It would then be important to understand the mechanisms by which the dissipated heat would be radiated away by the disc and any resulting changes to the vertical structure.

Equally important will be to identify the physical mechanism that causes the decrease in turbulent variability as we transition to the mesoscale regime. As it currently stands, our work suggests that the variability of an ionized accretion disc is tied to the global structure of the flow. These results, in combination with our results regarding the locality of angular momentum transport, suggests that attempts to interpret observations of accretion variability through local, viscous models of angular momentum transport (King et al. 2007; Ingram & Done 2011) could yield misleading conclusions regarding the physics of magnetized accretion discs. Future global simulations that incorporate boundary conditions and physics appropriate to a given astrophysical system are likely to be necessary to provide accurate interpretations regarding the variability of magnetized accretion discs.

Finally, the detection of density zonal flows in global calculations will be a very important avenue to pursue. As mentioned above, it will be necessary to determine whether these flows are an artifact of the shearing box approximation or are in fact present in global simulations as well. If they do exist in global calculations, we will need to quantify their radial (and azimuthal) scale as well as their amplitude relative to

the background density. Such quantifications will be important in informing models of planetesimal trapping and planet migration.

ACKNOWLEDGEMENTS

We thank Mitch Begelman, Charles Gammie, Julian Krolik, Omer Blaes, Shigenobu Hirose, Kareem Sorathia, Jim Stone, Xiao Yue Guan, Shane Davis, and John Hawley for useful discussions and advice. We also thank an anonymous referee for useful comments on an earlier draft of this paper. This work was supported by the NSF under grant numbers AST-0807471 and AST-0907872, and by NASA under grant numbers NNX09AB90G and NNX11AE12G. This research was supported in part by the NSF through TeraGrid resources provided by the Texas Advanced Computing Center and the National Institute for Computational Science under grant number TG-AST090106. We also acknowledge the Texas Advanced Computing Center at The University of Texas at Austin for providing HPC and visualization resources that have contributed to the research results reported within this paper. Computations were also performed on Kraken at the National Institute for Computational Sciences.

REFERENCES

- Armitage P. J., 1998, *ApJ*, 501, L189, [ADS](#), [arXiv:astro-ph/9805133](#)
- Balbus S. A., Hawley J. F., 1991, *ApJ*, 376, 214, [ADS](#)
- Balbus S. A., Hawley J. F., 1998, *Reviews of Modern Physics*, 70, 1, [ADS](#)
- Balbus S. A., Papaloizou J. C. B., 1999, *ApJ*, 521, 650, [ADS](#)
- Beckwith K., Armitage P. J., Simon J. B., 2011, *MNRAS*, pp 1130–+, [ADS](#)
- Blaes O., Krolik J. H., Hirose S., Shabaltas N., 2011, *ApJ*, 733, 110, [ADS](#), [1103.5052](#)
- Blaes O. M., Balbus S. A., 1994, *ApJ*, 421, 163, [ADS](#)
- Blandford R. D., Payne D. G., 1982, *MNRAS*, 199, 883, [ADS](#)
- Brandenburg A., Nordlund A., Stein R. F., Torkelsson U., 1995, *ApJ*, 446, 741, [ADS](#)
- Colella P., 1990, *Journal of Computational Physics*, 87, 171, [ADS](#)
- Colella P., Woodward P. R., 1984, *Journal of Computational Physics*, 54, 174, [ADS](#)
- Davis S. W., Stone J. M., Pessah M. E., 2010, *ApJ*, 713, 52, [ADS](#), [0909.1570](#)
- Evans C. R., Hawley J. F., 1988, *ApJ*, 332, 659, [ADS](#)
- Flock M., Dzyurkevich N., Klahr H., Turner N., Henning T., 2011a, *arXiv.org*, 1110, 961
- Flock M., Dzyurkevich N., Klahr H., Turner N. J., Henning T., 2011b, *The Astrophysical Journal*, 735, 122
- Fromang S., Papaloizou J., 2007, *A&A*, 476, 1113, [ADS](#), [arXiv:0705.3621](#)
- Fromang S., Papaloizou J., Lesur G., Heinemann T., 2007, *A&A*, 476, 1123, [ADS](#), [arXiv:0705.3622](#)
- Gammie C. F., 1998, in S. S. Holt & T. R. Kallman ed., *American Institute of Physics Conference Series Vol. 431 of American Institute of Physics Conference Series, Numerical models of accretion disks*. pp 99–107, [arXiv:astro-ph/9712233](#), [ADS](#)

- Gardiner T. A., Stone J. M., 2005, *Journal of Computational Physics*, 205, 509, [ADS](#), [arXiv:astro-ph/0501557](#)
- Gardiner T. A., Stone J. M., 2008, *Journal of Computational Physics*, 227, 4123, [ADS](#), [0712.2634](#)
- Goodman J., Xu G., 1994, *ApJ*, 432, 213, [ADS](#)
- Gressel O., Nelson R. P., Turner N. J., 2011, *MNRAS*, 415, 3291, [ADS](#), [1104.3987](#)
- Guan X., Gammie C. F., 2011, *ApJ*, 728, 130, [ADS](#), [1012.3789](#)
- Guan X., Gammie C. F., Simon J. B., Johnson B. M., 2009, *ApJ*, 694, 1010, [ADS](#), [0901.0273](#)
- Hawley J. F., 2000, *ApJ*, 528, 462, [ADS](#), [arXiv:astro-ph/9907385](#)
- Hawley J. F., Gammie C. F., Balbus S. A., 1995, *ApJ*, 440, 742, [ADS](#)
- Hawley J. F., Guan X., Krolik J. H., 2011, *ApJ*, 738, 84
- Hirose S., Krolik J. H., Blaes O., 2009, *ApJ*, 691, 16, [ADS](#), [0809.1708](#)
- Hirose S., Krolik J. H., Stone J. M., 2006, *ApJ*, 640, 901, [ADS](#), [arXiv:astro-ph/0510741](#)
- Hirose S., Turner N. J., 2011, *ApJ*, 732, L30, [ADS](#), [1104.0004](#)
- Ingram A., Done C., 2011, *MNRAS*, p. 1864, [ADS](#), [1108.0789](#)
- Johansen A., Youdin A., Klahr H., 2009, *ApJ*, 697, 1269, [ADS](#), [0811.3937](#)
- King A. R., Pringle J. E., Livio M., 2007, *MNRAS*, 376, 1740, [ADS](#)
- Lyra W., Johansen A., Klahr H., Piskunov N., 2008, *A&A*, 479, 883, [ADS](#), [0705.4090](#)
- Mignone A., 2007, *Journal of Computational Physics*, 225, 1427, [ADS](#), [arXiv:astro-ph/0701798](#)
- Miyoshi T., Kusano K., 2005, *Journal of Computational Physics*, 208, 315, [ADS](#)
- Nelson R. P., Gressel O., 2010, *MNRAS*, 409, 639, [ADS](#), [1007.1144](#)
- Noble S. C., Krolik J. H., Hawley J. F., 2010, *ApJ*, 711, 959, [ADS](#), [1001.4809](#)
- O'Neill S. M., Reynolds C. S., Miller M. C., Sorathia K. A., 2011, *ApJ*, 736, 107
- Pessah M. E., Goodman J., 2009, *ApJ*, 698, L72, [ADS](#), [0902.0794](#)
- Pringle J. E., 1981, *ARA&A*, 19, 137, [ADS](#)
- Sano T., Inutsuka S.-i., Turner N. J., Stone J. M., 2004, *ApJ*, 605, 321, [ADS](#), [arXiv:astro-ph/0312480](#)
- Shakura N. I., Sunyaev R. A., 1973, *A&A*, 24, 337, [ADS](#)
- Simon J. B., Armitage P. J., Beckwith K., 2011, *ApJ*, 743, 17, [ADS](#), [1107.3561](#)
- Simon J. B., Hawley J. F., 2009, *ApJ*, 707, 833, [ADS](#), [0906.5352](#)
- Simon J. B., Hawley J. F., Beckwith K., 2011, *ApJ*, 730, 94, [ADS](#), [1010.0005](#)
- Sorathia K. A., Reynolds C. S., Armitage P. J., 2010, *ApJ*, 712, 1241, [ADS](#), [1002.3611](#)
- Sorathia K. A., Reynolds C. S., Stone J. M., Beckwith K., 2011, *ArXiv e-prints*, [ADS](#), [1106.4019](#)
- Stone J. M., Gardiner T. A., 2010, *ApJS*, 189, 142, [ADS](#), [1006.0139](#)
- Stone J. M., Gardiner T. A., Teuben P., Hawley J. F., Simon J. B., 2008, *ApJS*, 178, 137, [ADS](#), [0804.0402](#)
- Yang C.-C., Mac Low M.-M., Menou K., 2011, *ArXiv e-prints*, [ADS](#), [1103.3268](#)